

1 **Geochronology of accessory allanite and monazite in the Barrovian**
2 **metamorphic sequence of the Central Alps, Switzerland**

3

4 Kate R. Boston¹, Daniela Rubatto^{1,2,3*}, Jörg Hermann^{1,2}, Martin Engi² and Yuri Amelin¹

5

6 1) Research School of Earth Sciences, Australian National University, Canberra,
7 ACT 2601 Australia

8

9 2) Institute of Geological Sciences, University of Bern, Baltzerstrasse 1-3, 3012
10 Bern, Switzerland

11

12 3) Institut de Sciences de la Terre, University of Lausanne, Bâtiment Géopolis, 1015
13 Lausanne, Switzerland

14

15 *Corresponding author: daniela.rubatto@geo.unibe.ch

16 **Abstract**

17 The formation of accessory allanite, monazite and rutile in amphibolite facies-
18 rocks across the Barrovian sequence of the Central Alps (Switzerland) was investigated
19 with a combination of petrography and geochemistry and related to the known
20 structural and metamorphic evolution of the Lepontine dome. For each of these minerals
21 a specific approach was adopted for geochronology, taking into account internal zoning
22 and U-Th-Pb systematics. In-situ U-Th-Pb dating of allanite and monazite by ion
23 microprobe revealed systematic trends for the ages of main deformation and
24 temperature in the Lepontine dome. Isotope dilution TIMS dating of rutile returns dates
25 in line with this picture, but is complicated by inheritance of pre-Alpine rutile and
26 possible Pb loss during Alpine metamorphism.

27 Allanite is generally a prograde mineral that is aligned along the main foliation of
28 the samples and found also as inclusions in garnet. Prograde allanite formation is
29 further documented by rutile inclusions with formation temperatures significantly
30 lower than the maximum T recorded by the rock mineral assemblage. Allanite ages vary
31 from 31.3 ± 1.1 Ma in orthogneisses in the East to 31.7 ± 1.1 Ma for a Bündnerschiefer
32 and 28.5 ± 1.3 Ma for a metaquartzite in the central area, to 26.8 ± 1.1 Ma in the western
33 part of the Lepontine dome. These ages are interpreted to date the main deformation
34 events (nappe stacking and isoclinal deformation of the nappe stack), close to peak
35 pressure conditions.

36 The timing of the thermal peak in the Lepontine dome is recorded in monazite that
37 grew at the expense of allanite and after a main episode of garnet growth at
38 temperatures of $\sim 620^\circ\text{C}$. Monazite in the central area yields an age of 22.0 ± 0.3 Ma,
39 which is indistinguishable from the age of 21.7 ± 0.4 Ma from a metapelite in the

40 western part of the Lepontine dome. In the central area some of the classical kyanite-
41 staurolite-garnet schists directly underlying the metamorphosed Mesozoic sediments
42 contain monazite that records only a pre-Alpine, Variscan metamorphic event of upper
43 greenschist to lower amphibolite facies-conditions dated at ~330 Ma.

44 The new age data provide evidence that nappe stacking at prograde amphibolite-
45 facies conditions and refolding of the nappe stack occurred between 32 and 27 Ma, only
46 a few million years after eclogite-facies metamorphism in the Adula-Cima Lunga unit.
47 Amphibolite-facies metamorphism lasted for about 10 My to ~22 Ma, allowing for
48 multiple ductile deformation and recrystallization events. The long lasting amphibolite-
49 facies metamorphism requires fast cooling between 20 and 15 Ma in the Central Alps.
50 This fast cooling was not related to an increase in sedimentation rates in the foreland
51 basins, suggesting that tectonic exhumation was responsible for termination of
52 amphibolite-facies metamorphism in the Lepontine dome.

53

54 **Keywords**

55 Accessory minerals; Barrovian metamorphism; Central Alps; ion-microprobe;
56 metamorphic petrology; SHRIMP; U-Pb dating.

57 **1. Introduction**

58 Well-constrained geochronology is essential for understanding metamorphic
59 processes that occur during orogenesis. Not only are ages of metamorphic events
60 important for establishing and correlating the timing of orogen-scale processes but
61 equally important is the rate at which these processes occur. Finding evidence of a
62 prograde history, crucial for evaluating models of heat transfer during orogenesis, is
63 often difficult because such evidence within a sample is usually obliterated by
64 subsequent, higher-grade metamorphism. Therefore, geochronology of Barrovian
65 metamorphic terranes is best achieved by combining different geochronometers that
66 are reactive under different conditions and thus may preserve different stages of the P-T
67 evolution. Allanite, monazite, and rutile (or titanate) are well-suited chronometers for
68 medium grade terrains, where the more reliable geochronometer zircon, is commonly
69 not reactive (e.g. Romer et al., 1996; Vonlanthen et al., 2012, see also a review in
70 Rubatto, 2017).

71 At upper greenschist-facies conditions, allanite can replace detrital or low-grade
72 metamorphic monazite; subsequently monazite crystallises at the expense of allanite at
73 middle amphibolite-facies conditions (e.g. Smith and Barreiro, 1990; Finger et al., 1998;
74 Wing et al., 2003; Janots et al., 2008; Kim et al., 2009). The reactions of monazite to
75 allanite and allanite to monazite do not take place in all rock types and at the same
76 conditions (Engi, 2017). The proposed variables controlling the reactions include bulk
77 composition (Finger et al., 1998; Wing et al., 2003; Janots et al., 2008; Spear, 2010), fluid
78 composition (Budzýn et al., 2010), the oxygen fugacity of the fluid (Janots et al., 2011),
79 and pressure (Janots et al., 2007; Spear, 2010). The use of allanite as U-Th-Pb
80 geochronometer is complicated by internal complexity (zoning) and typically high

81 concentration of initial Pb incorporated into the mineral during crystallisation (e.g.
82 Romer and Siegesmund, 2003). The problem of initial Pb in allanite has been addressed
83 by Gregory et al. (2007) and Smye et al. (2014). It has been demonstrated that
84 regression in a Tera-Wasserburg diagram or the Th-isochron technique (Gregory et al.,
85 2007) eliminates the need to assume the isotopic composition of initial Pb and allows
86 determination of geologically significant ages even for allanite with high amounts of
87 initial Pb (Janots and Rubatto, 2014). Additional issues with allanite are the relative
88 mobility of Th and U resulting in Th-U fractionation (Smye et al., 2014). Monazite and
89 allanite potentially incorporate excess of ^{206}Pb produced by the decay of ^{230}Th , which
90 can compromise the $^{206}\text{Pb}/^{238}\text{U}$ ratios. Therefore, calculation of isotopic ages and their
91 interpretation for these minerals demand special attention to these complications.

92 At amphibolite facies conditions, the stable Ti-bearing phase can be rutile, titanite
93 or ilmenite; their relative stability is controlled by pressure, temperature and bulk rock
94 composition. Rutile has the advantage that it generally does not incorporate initial Pb at
95 formation, but can contain very low U concentrations that render precise measurement
96 of radiogenic isotopic ratios difficult (Kooijman et al., 2010, Warren et al., 2012; Smye et
97 al., 2014).

98 Petrography is required to link the growth of accessory minerals to metamorphic
99 structures and major mineral phases (Janots et al., 2008; Janots et al., 2011; Regis et al.,
100 2014). The relative timing of monazite and allanite can also be linked to major phases
101 such as garnet through trace element distributions (e.g. Foster et al., 2002; Hermann and
102 Rubatto 2003; Buick et al., 2006). Both allanite and monazite commonly preserve
103 multiple growth zones, and individual growth zones can be analysed by *in situ*
104 techniques. Minerals that yield ages from more than one growth zone can be used for

105 inferring metamorphic rates, provided that metamorphic conditions can be established
106 for each growth zone (e.g. Hermann and Rubatto, 2003; Janots et al., 2009; Pollington
107 and Baxter, 2010; Rubatto et al., 2011; Janots and Rubatto, 2014; Regis et al., 2014).

108 The various challenges related to monazite, allanite and rutile geochronology (e.g.
109 multiple growth zones, common and inherited initial Pb, low U content, different
110 reactivity, etc...) may reduce accuracy and precision of single age determinations. A
111 mineral-specific approach to U-Th-Pb analysis and data treatment is required because of
112 the different U-Th-Pb systematics in monazite, allanite and rutile: bulk *versus* micro-
113 sampling methods according to internal zoning, U-Pb or Th-Pb system and different
114 approaches to corrections for initial Pb. Dating of multiple mineral zones in the same
115 rock and comparison of ages from diverse lithologies, both locally and over regional
116 scale will also increase reliability of the ages.

117 We apply the multi-mineral dating approach to the classical Barrovian, middle
118 grade sequence of the Lepontine Central Alps, Switzerland. This metamorphic sequence
119 has been the subject of half a century of study, following the reaction boundary maps of
120 Niggli and Niggli (1965). Geochronology studies in the area date back four decades to
121 the pioneering work of Hunziker, Jäger, Köppel and Steiger (Hunziker, 1969; Jäger,
122 1973; Köppel and Grünenfelder, 1975; Deutsch and Steiger, 1985; Steck and Hunziker,
123 1994). Despite the long history of geochronology there remain significant uncertainties
124 and debates on the timing and duration of Barrovian metamorphism. The lack of
125 consensus is mainly due to uncertainty regarding the extent to which dated micas and
126 amphibole represent inherited, formation or cooling ages considering the metamorphic
127 grade and complex metamorphic history preserved the rocks in the Central Alps (parts
128 of which span two or more orogenic cycles). The present study is focused on areas

129 between the Northern and Southern Steep Belts, encompassing almost the entire East-
130 to-West breadth of the Lepontine dome.

131

132 **2. Geological background**

133 The Lepontine dome of the Central Alps extends between the Northern and
134 Southern Steep Belts (NSB and SSB respectively), the Simplon line in the west, and
135 Bergell area in the east (Fig. 1). The nappe stack in the dome comprises
136 polymetamorphic basement units and Mesozoic sedimentary cover units; both are
137 overprinted by a Barrovian sequence that reached maximum temperatures just north of
138 the Insubric line (e.g. Frey et al., 1974; Frey et al., 1980; Trommsdorff, 1980; Engi et al.,
139 1995; Todd and Engi, 1997). Concentric isograds and isotherms document an increase in
140 metamorphic grade from lower-amphibolite facies in the Northern Steep Belt (NSB) to
141 upper-amphibolite facies with partial melting in the Southern Steep Belt (SSB, Fig. 1b).

142 This study investigates metasediments from the cover sequences as well as
143 basement rocks (Table 1). The Permo-Mesozoic sedimentary units were deposited on
144 the subsiding European continental margin during the extensional phase in between the
145 Variscan and Alpine orogenies (Grujic and Mancktelow, 1996; Berger et al., 2005;
146 Garofalo, 2012). During Alpine metamorphism the peak temperature was reached after
147 nappe formation and emplacement, as mineral zone boundaries and isotherms
148 discordantly crosscut tectonic boundaries (Fig. 1b; Niggli and Niggli, 1965; Frey et al.,
149 1980; Engi et al., 1995; Todd and Engi, 1997). In the southern portion of the Lepontine
150 dome, Barrovian metamorphism is considered to be syn- to post-kinematic with
151 refolding of the established nappe pile and exhumation of some high-pressure rocks
152 (Frey et al., 1980; Nagel et al., 2002; Brouwer et al., 2004; Brouwer et al., 2005; Berger et

153 al., 2005; Rützi et al., 2008; Berger et al., 2011). In the northern part of the Lepontine,
154 Barrovian metamorphism probably reached T_{\max} conditions after most of the major
155 thrusts ceased to operate (Berger et al., 2005; Wiederkehr et al., 2008; Janots et al.,
156 2009; Wiederkehr et al., 2009; Berger et al., 2011). However, Wiederkehr et al. (2011)
157 showed that near the NE-margin isotherms are steeply inclined, affected by late-
158 orogenic km-scale folding, and may be displaced along a major nappe boundary (in the
159 footwall of the Adula thrust sheet). In the study area, Barrovian metamorphic conditions
160 reached temperatures of 550-650 °C and pressures of 7 kbar or less at peak temperature
161 (Engi et al., 1995; Todd and Engi, 1997).

162 The age of Barrovian metamorphism in the Central Alps is the subject of ongoing
163 debate. Pioneering studies on mica geochronology (K-Ar, Rb-Sr) from outside the
164 Lepontine dome, where peak metamorphic temperatures did not exceed the assumed
165 closure temperature of the dated minerals, led to a long dominating view that placed
166 peak Barrovian metamorphic conditions at 38-40 Ma (Jäger, 1973; Steck and Hunziker,
167 1994). On the other hand, K-Ar dating of amphiboles across the northern part of the
168 Lepontine dome returned much younger ages of 32-23 Ma that were interpreted as
169 formation ages (Deutsch and Steiger, 1985). Such younger metamorphic ages had been
170 previously documented in monazite from the centre of the Lepontine dome (Köppel and
171 Grünenfelder, 1975) but no relation of monazite age to metamorphic assemblage was
172 shown. More recent work emphasised crystallisation ages of accessory minerals, and
173 this now points to a younger age (17-32 Ma) for Barrovian metamorphism and an age
174 gradient across the belt (e.g. Janots et al., 2009; Rubatto et al., 2009; Berger et al., 2011).
175 *In situ* zircon and allanite ages for protracted melting in migmatites from the SSB span
176 from ~ 32 to 22 Ma, indicating that temperatures were high in the southernmost part of
177 the Lepontine dome up to 22 Ma (Rubatto et al., 2009; Gregory et al., 2012). Similarly,

178 studies on rocks in the northern limits of the Lepontine dome have established an 18-19
179 Ma age for T_{\max} (Janots et al., 2009). Based on U-Pb in monazite, this young age for T_{\max}
180 is supported by 15-18 Ma Ar-Ar ages in white mica in rocks in the north-east of the
181 Lepontine Dome (Wiederkehr et al., 2009) and in the Lucomagno area (Allaz et al.,
182 2011).

183 The modern geochronology studies have mainly focussed on areas in the Southern-
184 and Northern Steep Belts (Gebauer 1996; Romer et al., 1996; Janots et al., 2009; Rubatto
185 et al., 2009; Wiederkehr et al., 2009), and data from the central part of the dome remain
186 scarce. In this area, zircon was largely unreactive under medium grade metamorphic
187 conditions and indeed our attempt to date the rare and thin zircon metamorphic
188 overgrowths only returned scattered dates that do not represent significant ages.
189 Systems utilising micas (e.g. K-Ar, Ar-Ar, Rb-Sr) have been interpreted to largely record
190 cooling, retrograde reactions, or they retain pre-Alpine relics (e.g. Jäger, 1973; Hurford
191 1986; Janots et al., 2009; Allaz et al., 2011).

192

193 **3. Sample description and petrography of accessory minerals**

194 Sample locations of this contribution are from as far north as Campolungo (south-
195 east of Airolo, Fig. 1b); the Western-most sample is from Croveo, north of Domodossola.
196 Eastern-most samples are from the Forcola area, ~ 75 km east of Croveo and west of
197 Chiavenna. The geographical spread of samples across this central part of the Lepontine
198 dome provides ages that can reconcile the data sets of the NSB and SSB.

199 Our samples in the central Lepontine dome record sub-solidus amphibolite-facies
200 conditions during Barrovian metamorphism. For the same area, Todd and Engi (1997)
201 reported, T_{\max} varying from 550°C in the lower grade rocks, to 620°C in the highest-

202 grade samples. Pressures estimated for equilibration of the rocks (i.e. at maximum T)
203 vary between 5 kbar in the eastern-most samples and < 6.5 kbar in samples in the
204 central to western part of the study area (Todd and Engi, 1997). An overview of sample
205 locations, mineral assemblages and geochronology is presented in Table 1. Details of the
206 mineral textures and compositions are presented in the electronic Appendix. Important
207 textural relationships regarding key major and accessory minerals are shown in Fig. 2.
208 Bulk rock analyses of the samples – excluding sample Sp9312, which has distinct
209 compositional layering – are given in Table A1.

210

211 **4. Mineral composition**

212 *4.1. Garnet*

213 Croveo schist (Ma9330) garnet grains have core-rim compositional zoning (Fig. 4a,
214 Table A2). Garnet cores are rich in Mn and Ca (MnO = 5.8 wt%; CaO = 8.1 wt%), which
215 decrease towards the rims. Fe and Mg have the opposite trend, with lowest
216 concentrations in the core (FeO = 27 wt%; MgO = 0.85 wt%), increasing outwards. The
217 HREE and Y concentrations are highest in the core (Y = 370 ppm, Yb = 96 ppm) and
218 decrease dramatically before increasing again towards the outer rim. The increase in
219 HREE+Y in the outer rim is taken to indicate garnet resorption. HREE patterns are
220 steepest in the core ($Dy_N/Lu_N = 0.03$) and become flatter outwards ($Dy_N/Lu_N \leq 1.4$).
221 Garnet outer rims are characterised by a flat to negative HREE slope ($Dy_N/Lu_N > 2$, Fig.
222 4b). Garnet cores and rims have a weak negative Eu anomaly of = 0.4-0.7.

223 Garnet grains in CLB-3 Campolungo calcschist show a simple core-to-rim zoning in
224 the inner part of the garnet (Grt I) with some subtle complexity in the grain rim, (Grt II,
225 Fig. 4c). CLB-3 Grt I cores are rich in Mn (MnO = 2.3 wt%) and poor in Mg (MgO = 1.6

226 wt%) compared to Grt II (MnO = 0.4 wt%; MgO = 2.4 wt%). Garnet grains in this sample
227 are remarkably low in REE (Fig. 4d, Table A2). LREE concentrations were often below
228 the limit of detection (typically 0.002 ppm for Ce, 0.003 ppm for La), and only REE
229 heavier than Eu were consistently above detection limits. HREE slopes are steep in Grt I
230 cores ($Dy_N/Lu_N = 0.008$) and become gentler outwards ($Dy_N/Lu_N = 0.15$ near Grt II). Grt
231 II is characterised by relative enrichment in some HREE, particularly Tb to Er.

232 Garnet in sample CLM-5 and 6 has a distinct core that is rich in inclusions of
233 graphite. The inclusion-poor rim is separated from the core by an irregular annulus that
234 cuts across the zoning of the core (Fig. 4e-f). The core is poor in MgO (1-4-2.5 wt%) and
235 richer in CaO (0.7-2.6 wt%) and MnO (0.7-4.2 wt%) with respect to the rim (MgO = 3.0-
236 3.5, CaO = 0.4, MnO = 0.13-0.4 wt%). The large core generally shows a decrease in these
237 elements from the inner to the outer part, and additional Mn and Ca patchy zoning in
238 CLM-5 or oscillatory zoning in CLM-6 (Fig. 4f). The core of CLM-6 garnet contains
239 inclusions of chloritoid ($X_{Mg}=0.14$), rare staurolite ($X_{Mg}=0.07$), chlorite, quartz, ilmenite
240 and rutile. The discordant rim is more homogeneous in composition with a slight
241 increase in Mg outwards. Ilmenite, rutile, chlorite, quartz and rare chloritoid ($X_{Mg}=0.19$)
242 inclusions have been observed. Staurolite in the matrix coexists with garnet rims and
243 displays significantly higher $X_{Mg}=0.21$ than staurolite inclusions.

244 Alpe Sponda fels Sp9712 contains garnet with complex zoning in major and trace
245 element composition. Because garnet grains are scarce in Sp9712, they were analysed as
246 polished grains retrieved from the sample separate. Ca element maps of larger grains
247 show an outward increase in Ca from the core (Grt I), before an abrupt drop in
248 concentration in Grt II (Fig. 4g). A number of garnet grains show embayment to the Ca
249 zoning. In these grains, Fe shows a complementary trend to Ca, decreasing from the core

250 before increasing in Grt II. The trace element zoning is best seen in HREE
251 concentrations. Grt I cores display little zoning (Fig. 4g) and have a flat HREE pattern.
252 Towards the rim of Grt I the HREE significantly decrease. Grt II is marked by an increase
253 in HREE to higher levels than what is observed in Grt I cores, followed by a decrease
254 towards the rims of Grt II.

255 One small (200 μm diameter) euhedral garnet grain with distinctive composition
256 (Grt III) presents a relatively simple, bell-shaped zoning with cores enriched in Ca and Y,
257 which decrease towards the rims. HREE are even more extremely enriched than in Grt II
258 ($\text{Dy}_\text{N}/\text{Lu}_\text{N} = 0.1\text{-}0.4$, Fig. 4h) with greatest HREE enrichment occurring in the core. Y
259 concentration is as high as 3 wt % in garnet cores and decreases to ~ 3500 ppm at the
260 rim. Element maps of major and trace elements suggest that Grt II and Grt III formed at
261 the same time, with the first one as overgrowth on pre-existing, partially resorbed cores
262 and the latter as newly formed, small individual grains.

263 4.2. *Allanite*

264 *Metasediments.* The compositional zoning of allanite is similar in the metasediment
265 samples from the western and central areas (Robiei Ba0901, Campolungo CLB-3 and
266 Ma0901); they are considered here together. Allanite has three distinctive zones: a
267 LREE-enriched core, a HREE-enriched mantle, and an epidote rim (Fig. 3a-d). Ba0901
268 has one additional allanite rim that is overgrown on epidote.

269 Robiei (Ba0901) LREE-allanite cores and rims have similar REE patterns (Fig. 5a)
270 with a significant negative Eu anomaly ($\text{Eu}/\text{Eu}^* = 0.3\text{-}0.5$ in cores and $0.2\text{-}0.5$ in rims)
271 and a similar HREE slope ($\text{Dy}_\text{N}/\text{Lu}_\text{N} = 4.5$ in cores and 5.5 in rims). Ba0901 allanite cores
272 vary in Th from 4300 to 12000 ppm, U spans from 600 to 1500 ppm, and Th/U ratio
273 varies from 2.8 to 12 (Table A4). Ba0901 LREE-allanite rims are similar in composition

274 to cores of the same grains but differ in the abundance of HREE, which tend to be higher
275 in the rims than cores. Th concentration is lower in rims (2000-8000 ppm) and U
276 concentration is similar to cores (300-1700 ppm). Th/U ratios show little variation, with
277 Th/U between 3.5 and 6.5 in allanite rims.

278 Samples from Campolungo (CLB-3 calcschist and Ma0901 quartzite, Fig. 3c-d) both
279 lack the LREE-rich rim characteristic of the Robiei (Ba0901) allanite. The REE patterns
280 of allanite cores in both samples have a significant negative Eu anomaly ($\text{Eu}/\text{Eu}^* = 0.6$ in
281 CLB-3 and 0.5 in Ma0901) and a steep HREE pattern (CLB-3 $\text{Dy}_\text{N}/\text{Lu}_\text{N} = 7-17$, Ma0901
282 $\text{Dy}_\text{N}/\text{Lu}_\text{N} = 8-24$; Fig. 5b-c). CLB-3 calcschist allanite cores have lower Th and U
283 concentrations than in the quartzite (Ma0901). CLB-3 allanite cores contain 4300-7700
284 ppm Th and 100-400 ppm U; Ma0901 allanite contains 3300-18000 ppm Th and 400-
285 1200 ppm U. Th/U ratios in CLB-3 are high and vary from 40 to 77; Th/U ratios in
286 Ma0901 quartzite vary from 2.8 to 27.

287 Allanite mantles with a relative HREE- and U-enrichment (Fig. 5d) are only found
288 in the metasediments. The HREE-allanite mantles are commonly thin and can have
289 complex internal zoning, especially in the case of Ba0901 (Fig. 3a-b). In all allanite
290 mantle zones, HREE concentrations decrease outwards. Campolungo allanite from both
291 CLB-3 calcschist and Ma0901 quartzite has significant HREE enrichment in the mantle
292 zone, and the HREE pattern has a concave down shape (Fig. 5b-c). HREE-allanite from all
293 samples shows a similarly weak negative Eu-anomaly ($\text{Eu}/\text{Eu}^* \approx 0.75$). U concentrations
294 are much lower in the Campolungo calcschist than the quartzite (500 to 2300 ppm in
295 CLB-3 calcschist and 1200 to 3500 ppm U in Ma0901); Th/U ratios in mantle allanite are
296 much lower than in the cores for both samples (CLB-3 Th/U = 2-3; Ma0901 Th/U = 0.4-
297 1).

298 *Forcola orthogneiss*. Despite the great variety of internal textures (Fig. 3f-h),
299 allanites from orthogneiss samples (LEP0979, LEP0980, LEP0807) have similar trace
300 element compositions. For all Forcola orthogneiss allanites, REE patterns have
301 significant negative Eu anomalies ($\text{Eu}/\text{Eu}^* = 0.1\text{-}0.6$, Fig. 5e-f) and a comparable HREE
302 slope with $\text{Dy}_\text{N}/\text{Lu}_\text{N}$ varying from 2 to 18. Th concentrations in orthogneiss allanites vary
303 from 2000 to 20000 ppm; U concentration spans from 400 to 1200 ppm. The highest U
304 concentrations occur in patchy allanite in sample LEP0807. Th/U ratios typically span
305 between 4 and 31 in LEP0979 and LEP0807 allanites. LEP0980 regularly zoned allanite
306 of Alpine age have a much lower Th/U ratio ($\text{Th}/\text{U} = 0.2$ to 12). The spectacularly zoned
307 LEP0980 mosaic allanite have a trace element composition that is not distinctive and is
308 within the range of the other Forcola orthogneiss allanites.

309 *5.4. Monazite*

310 REE composition of monazite is very similar in both samples (Croveo schist
311 Ma9330, Alpe Sponda fels Sp9712) with a negative Eu anomaly ($\text{Eu}/\text{Eu}^* 0.5\text{-}0.4$) and a
312 variable HREE slope (Fig. 5g, Table A5). U concentrations are similar in both samples
313 (Ma9330 U = 3900-6300 ppm; Sp9712 U = 5400-6600 ppm) and Th concentrations are
314 all but identical (Ma9330 Th = 21.8-34.1 %; Sp9712 Th = 25.2-34.7 %). Th/U ratios tend
315 to be higher and more variable in Ma9330 monazite than in that from Sp9712 (Ma9330
316 $\text{Th}/\text{U} = 5.0\text{-}7.9$; Sp9712 $\text{Th}/\text{U} = 4.6\text{-}6.3$).

317

318 **5. Rutile geothermometry**

319 Selected rutiles were analysed for trace elements using LA ICP-MS (Table A3). The
320 Zr content of rutile is a geothermometer (Ferry and Watson, 2007) that can provide
321 crystallisation temperature estimates for the rutiles that are related to the growth of

322 allanite cores (and hence their age) in Ma0901 quartzite and to the rutile bearing-
323 paragenesis and/or ages in samples Ma9330, Ba0903A, CLB-3, CLB-4 and Sp9712.
324 Following Ewing et al. (2013), the sources of uncertainty to be propagated onto Zr-in-
325 rutile temperature estimates are the effect of analytical uncertainty of Zr measurement
326 and uncertainty inherent in the calibration ($\sim 3\%$ for 500 °C, Ferry and Watson, 2007).
327 The Zr analytical error was conservatively estimated to be $\pm 15\%$, which corresponds to
328 an error of $\pm 10\text{-}15\text{ }^\circ\text{C}$ for the 500-650 °C temperature range and combined with the
329 internal error of the calibration of Ferry and Watson (2007) it gives a total uncertainty
330 of $\pm 20\text{ }^\circ\text{C}$ for these samples.

331 Rutile from sample Ma9330, the western-most sample, returns a Zr-in-rutile
332 temperature of $\sim 565\text{ }^\circ\text{C}$ (Zr = 100 ppm), clearly lower than T_{max} of 620 °C from Todd
333 and Engi (1997). Ba0903A is of significantly lower grade than Ma9330 (T_{max} for this area
334 is 575 °C, Todd and Engi, 1997) and the range of Zr concentrations in rutile from 100 to
335 166 ppm, corresponds to 565-595 °C. Samples CLB-3, CLB-4 and Ma0901 are all from
336 the same locality and return Zr-in-rutile temperature estimates of $\sim 565\text{ }^\circ\text{C}$, 625 °C and
337 580 °C, respectively (Zr = 100, 240 and 130 ppm, respectively). Sp9712 is the eastern-
338 most rutile-bearing sample and returns a Zr-in-rutile temperature estimate of 550 °C (Zr
339 = 85 ppm), which is again below the T_{max} expected for this area according to Todd and
340 Engi (1997).

341

342 **6. Geochronology**

343 Depending on the assemblages of the investigated samples, monazite, allanite or
344 rutile were dated. These minerals have different Th-U contents (rutile is virtually Th free
345 and contains only 0.3 to 20 ppm U, monazite has Th/U of 5–10 and Alpine allanite has

346 Th/U of 2–80) and can variably incorporate initial Pb. Additionally, rutile shows no
347 evident internal zoning, monazite shows limited evidence of internal zoning, whereas
348 allanite is strongly zoned in both composition and age. Because of these inherent
349 differences, geochronology of these minerals followed different approaches to achieve
350 best age accuracy and precision.

351 Rutile was dated by ID-TIMS because of its low U content and the lack of intragrain
352 zoning. Due to low U content, the measured Pb composition has a low radiogenic
353 component and a significant proportion of initial Pb (Supplementary Table A8). Because
354 these are multigrain fractions from different samples, with apparent different age they
355 cannot be used for an isochron calculation and the best way to determine the initial Pb
356 composition for each aliquot was to measure the composition of low-U-feldspar (Table
357 A8b).

358 In the investigated samples, allanite is rich in Th and U, and both systems are
359 strongly contaminated by initial Pb. The Th-Pb system in these samples is relatively
360 more radiogenic than U-Pb (Supplementary Table A7) and thus it was preferred for age
361 determination. Measuring the Pb composition of feldspar is not a rigorous approach to
362 estimate the initial Pb composition for allanite in these samples because of the zoning
363 complexity, the presence of different age populations, and the possibility of inherited
364 initial Pb from precursor monazite (e.g. Romer and Rötzler, 2011). A better approach is
365 to calculate Th-isochrons according to the methods of Gregory et al. (2007; $^{208}\text{Pb}/^{206}\text{Pb}_c$
366 versus $^{232}\text{Th}/^{206}\text{Pb}_c$ where $^{206}\text{Pb}_c$ is initial Pb only) for multiple analyses of the same
367 domain in each sample. In this approach the assumption on common Pb composition
368 (adopted to be the model composition of Stacey and Kramers 1975) has only marginal
369 bearings on the calculation of the $^{206}\text{Pb}_c$ (see Gregory et al., 2007; Janots and Rubatto,
370 2014).

371 In monazite, unlike allanite, the initial Pb incorporation is low (mostly <3%) and
372 thus the assumption on the common Pb composition has no bearing on the age within
373 uncertainty. The U-Pb system was preferred to the Th-Pb system because of analytical
374 setup (see methods).

375 *6.1. Western Samples: Croveo (Ma9330) and Robiei (Ba0901)*

376 Alpine ages are summarised in Fig. 6 and data are presented in Tables A5-A7.
377 Monazite is the only accessory phase dated in the western-most sample Ma9330. The
378 monazite grains are unzoned in BSE images and return a $^{206}\text{Pb}/^{238}\text{U}$ age of 21.7 ± 0.4 Ma
379 (95 % confidence for all average ages, Fig. 7b) that is within error of the monazite age
380 from central sample Sp9712 (see below).

381 Accessory allanite was dated in the Robiei sample Ba0901. Pre-Alpine igneous
382 allanite relics returned dates that span from 397 to 187 Ma, a spread that may indicate
383 alteration or partial resetting of the ^{232}Th - ^{208}Pb isotopic system. Metamorphic allanite
384 cores return an isochron age of 26.8 ± 2.3 Ma (MSWD = 2.0, n = 9/10; Fig. 8a). The
385 scatter in the data is likely to be due to some minimal overlap of the SHRIMP analysis
386 spot onto the surrounding growth zones, because of the small size of the cores. Allanite
387 rim analyses define an isochron age of 19.7 ± 1.3 Ma (MSWD = 0.77, n = 11/12; Fig. 8b).

388 Rutile from Ba0903A calcschist returns a range of dates for different fractions that
389 scatter from 21 to 27 Ma (Table A8). The oldest rutile date is from fraction A45 40, at
390 27.4 ± 1.7 Ma, which is similar to that of allanite cores from the same locality (Ba0901).
391 Two fractions of orange grain fragments returned dates of 21.5 ± 2.5 Ma and 26.1 ± 2.2
392 Ma.

393 6.2. Central samples: Campolungo (CLM-5, CLM-6, CLB-3, CLB-4, Ma0901) and Alpe Sponda
394 (Sp9712)

395 Ages from allanite and monazite were extracted from the central samples (Fig. 6).
396 Monazite in sample CLM-5 and 6 is pre-Alpine in age despite being aligned along the
397 main foliation. They have weak internal zoning with sector and flame texture. Both
398 samples returned a majority of dates between 322 and 339 ± 4 Ma (1σ) that define
399 average ages of 331 ± 4 Ma and 326 ± 4 , respectively (Fig. 7a). In both samples a few
400 analyses show scattering towards younger dates that likely reflect Pb disturbance
401 during Alpine overprint.

402 Allanite from CLB-3 calcschist returns an isochron age of 31.7 ± 1.1 Ma (MSWD =
403 1.5, $n = 15/17$, Fig. 8c), which is older than Ma0901 allanite cores from the same locality
404 (28.5 ± 1.3 Ma, MSWD = 0.60, $n = 27/29$, Fig. 8d). Notably, for both samples, the
405 weighted means of the most significant cluster of single spot dates – corrected for Pb,
406 using the model common Pb composition of Stacey and Kramers (1975) – are within
407 error of the isochron ages (CLB-3 mean age 31.8 ± 0.9 Ma, MSWD = 1.7, N 10; Ma0901
408 29.6 ± 0.5 Ma, MSWD = 1.2, N 16). However, for the reasons given by Gregory et al.
409 (2007) and Janots and Rubatto (2014), the isochron ages are deemed more reliable and
410 are used in the discussion. Ma0901 HREE-rich allanite mantles are large enough to be
411 analysed by SHRIMP but contained prohibitively high f_{208} (> 90%) and the data do not
412 form a reliable isochron, preventing a reliable age calculation.

413 Rutile dates from one Campolungo sample (CLB-4) span from 19 to 25 Ma (Table
414 A8). Like Ba0903A rutiles, the fractions comprising dark-coloured and larger grains and
415 fragments tend to be older (~ 24 Ma, 4 fractions; Table A8) than the lighter honey-
416 coloured rutile grains (~ 21 Ma, 3 fractions).

417 Sp9712 monazite returns a $^{206}\text{Pb}/^{238}\text{U}$ age of 22.0 ± 0.3 Ma (Fig. 7c; Table A6).
418 Monazite grains are subtly heterogeneous in BSE images (Fig. 7c), but there is no
419 correlation between zoning and age. The monazite age is within error of the monazite
420 age from Ma9330. Two groups of dates were obtained from Sp9712 rutile (Table A8).
421 Dark red-brown rutiles returned older dates between 52 and 57 Ma; the apparently
422 younger rutiles are orange and light honey-coloured grains at 33.45 ± 0.37 Ma (Table
423 A8).

424 *6.3. Eastern samples: Forcola Orthogneiss (LEP0979, LEP0980, LEP0807)*

425 Two orthogneiss samples contain metamorphic allanite that return acceptable
426 isochron ages (MSWD < 2). Subgrain cores from LEP0980 mosaic allanite return an
427 isochron age of 31.3 ± 1.1 Ma (MSWD = 1.1, n = 16/16; Fig. 8e); allanite from LEP0807,
428 the structurally shallowest Forcola sample, return an isochron age of 27.4 ± 0.6 Ma
429 (MSWD = 1.9, n = 17/21; Fig. 8f).

430 Allanite samples that did not form meaningful isochrons (MSWD > 2) are LEP0979
431 allanite, regularly zoned LEP0980 allanite, and subgrain rims of LEP0980 mosaic
432 allanite. For these sample ^{207}Pb -corrected single spot dates are presented in Table A7,
433 and in all cases they show a range of several Ma, suggesting the isotopic systematic was
434 disturbed or individual grains contained variable initial Pb. Such dates are not taken
435 individually to constrain significant geological events.

436

437 **7. Discussion**

438 *7.1. Reliability of ages*

439 At low to medium metamorphic grade allanite and monazite can replace each
440 other (Janots et al., 2008; Janots et al., 2009) or grow from previous magmatic allanite or

441 monazite with possible incorporation of radiogenic Pb from the precursor phase (e.g.
442 Romer and Siegesmund, 2003; Romer and Rötzler, 2011). This inheritance has bearings
443 on initial Pb composition and thus age calculation. For the analysed monazite the
444 fraction of initial Pb is small enough to make this problem minimal. Any incorporation of
445 inherited radiogenic Pb would imply a lower $^{207}\text{Pb}/^{206}\text{Pb}$ ratio of the initial Pb and
446 mildly shift the calculated age to younger values. Notably any excess ^{206}Pb may lead to a
447 shift to older ages (see below).

448 For allanite the presence of inherited radiogenic and common Pb is a more serious
449 problem, but the Th-isochron calculation is largely independent from the initial Pb
450 composition, which is only used to determine the fraction of initial ^{206}Pb (see Gregory et
451 al., 2007). Additionally, in the sample investigated, single spot ages calculated assuming
452 a secular Pb composition (Stacey and Kramers, 1975) are mostly close to the Th-
453 isochron age, indicating that initial Pb incorporated at growth was generally non
454 radiogenic. This observation also limits the possibility of a shift in the age due to
455 chemical inheritance as described by Romer and Siegesmund (2003) and Romer and
456 Rötzler (2011). For allanite domains that do not yield an isochron age, the range of
457 single spot dates are not given a geological significance as they may be affected by Pb
458 inheritance. This is likely the case for the mosaic allanite in orthogneiss LEP0980 (Fig.
459 3h), where the subsolidus reaction that recrystallized the pre-Alpine allanite into the
460 mosaic Alpine allanite was likely a closed system reaction and thus the Pb did not
461 equilibrate.

462 Excess ^{206}Pb due to the incorporation of ^{230}Th at growth is another issue to
463 consider in dating Th-rich minerals. Unlike magmatic systems, in metamorphic rocks a
464 correction for excess ^{206}Pb based on the Th/U of the system is not possible because of
465 changing reactive bulk during metamorphism. While this does not affect the Th-Pb

466 system used for allanite dating, it can produce apparently older $^{206}\text{Pb}/^{238}\text{U}$ ages for
467 monazite. Unlike magmatic monazite grown from a melt, excess ^{206}Pb in metamorphic
468 monazite has been rarely reported (see Rubatto et al., 2013; Wang et al., 2015).
469 Monazite analyses in this study are concordant within analytical uncertainty and this
470 indicates that any excess ^{206}Pb is less than the analytical uncertainty of the $^{206}\text{Pb}/^{238}\text{U}$
471 ratio of single analyses, that is 0.6–1.5% for Variscan monazite and 2–4% in Alpine
472 monazite.

473 In all analysed samples, rutile U contents are low, (mostly below 15 ppm with the
474 exclusion of sample CLB where U content is 26-36 ppm, Table A3) and the proportion of
475 initial Pb is thus high, with molar fraction of non-radiogenic ^{206}Pb between 0.75 and 0.98
476 (Table A8). To attempt non-radiogenic Pb correction, the Pb composition of K-feldspar
477 was measured in sample CLB4 and Sp9712, but a precise estimate was only obtained for
478 Sp9712. Using this feldspar Pb composition to correct the data results in dates scattering
479 from ~ 20 to 54 Ma. However, particularly the dates above 23 Ma have a positive
480 correlation to the fraction of non-radiogenic Pb, an indication that the chosen initial Pb
481 isotopic composition may be not representative for the rutile. Applying this initial Pb
482 correction, the resulting rutile dates are mostly Alpine with a suspected pre-Alpine
483 component in the Alpe Sponda basement (see further discussion below). The U-Pb
484 analyses do not form a well defined regression in an uncorrected Tera Wasserburg plots,
485 and thus the composition of the initial Pb could not be calculated by this method. Pb-Pb
486 isochrons also failed due to data scatter. Because of the low Pb radiogenic component in
487 the rutile and the issue with initial Pb correction, the rutile U-Pb dates should be used
488 and interpreted with extreme caution. Whenever possible, we prefer to rely on more
489 robust age data from other mineral chronometers

490

491 *7.2. Conditions of allanite, monazite and rutile formation*

492 Constraining the condition of formation of allanite and monazite with respect to
493 structures and metamorphism is crucial for age interpretation. During Alpine
494 metamorphism, the peak temperatures were below 650°C in all investigated samples
495 (Fig. 1), which is well below the closure temperature for the Th-U-Pb system in allanite
496 (Gregory et al., 2012) and monazite (Rubatto et al., 2001). This is further confirmed for
497 allanite by the presence of inherited ages in the Forcola orthogneisses and the Robiei
498 gneiss Ba0901. Therefore, the obtained ages date the formation of the mineral growth
499 zones. We use textural relationships and the trace element composition of monazite and
500 allanite growth zones to constrain the reactions that took place during allanite-epidote
501 growth and infer coexistence of accessory minerals and major phases such as garnet
502 (e.g. Rubatto, 2002; Hermann and Rubatto, 2003; Buick et al., 2006). Zr-in-rutile
503 thermometry can be used to relate rutile ages to metamorphic conditions. However, in
504 the present case, age interpretation is complicated by the potential mixing of different
505 rutile generations when 100s of grains are picked for isotope dilution analysis and the
506 fact that Pb diffusion in rutile may occur at amphibolite-facies conditions over the
507 relatively wide range of ~450 to 650 °C (e.g. Cherniak, 2000; Vry and Baker, 2006;
508 Kooijman et al., 2010; Warren et al., 2012). Below we discuss the ages from across the
509 area in chronological order, starting from Variscan metamorphic ages in the basement
510 before discussing prograde Alpine allanite to higher temperature monazite.

511 Pre-Alpine monazite in Campolungo schists CLM-5 and 6 is aligned along the
512 folded main foliation (Fig. 2e), which is partly wrapping the garnet, but is overgrown by
513 staurolite and kyanite. In both samples monazite contains black micro inclusions of
514 graphite, which occasionally defines a foliation that continues in the matrix (Fig 2c). This
515 suggests that the Carboniferous monazite already formed as part of a metamorphic

516 assemblage. The crystals are euhedral, flat prismatic in shape, with sharp edges and
517 yield a single age and therefore a detrital origin is excluded. The ~330 Ma age in the two
518 samples is interpreted as dating Variscan metamorphism in the Campolungo (Simano
519 nappe) basement. It is surprising that no Alpine monazite has been found in both
520 samples. Garnet in CLM-6 displays a core with concentric zoning that is separated from a
521 nearly homogenous rim by an irregularly shaped annulus that is crosscutting the core. In
522 the light of a pre-Alpine age of metamorphic monazite, this feature is interpreted as a
523 phase of garnet resorption between the Variscan metamorphic event and the Alpine
524 amphibolite-facies metamorphism. Accordingly, the Variscan metamorphic conditions
525 can be constrained to be of upper greenschist to lower amphibolite facies based on the
526 inclusion assemblage of chloritoid, chlorite and staurolite found in the garnet core. At
527 these general conditions, rutile may have been the stable Ti phase. Formation of rutile
528 during a Variscan event is suggested on the basis of the high apparent ages obtained in
529 Alpe Sponda fels Sp9712, where two fractions containing darker rutile grains returned
530 dates of ~ 52 to 57 Ma. Such spurious dates could be due to mixing between Alpine and
531 Variscan rutile, possibly with partial Pb loss of the older population.

532 The pre-Alpine metamorphic event was overprinted during Alpine metamorphism
533 by the amphibolite-facies assemblage of muscovite-biotite-garnet-staurolite at only
534 slightly higher metamorphic conditions. The main foliation S1 in schists CLM-5 and 6,
535 that is parallel to the main foliation in the overlying metamorphosed Mesozoic
536 sediments, is therefore interpreted as a transposed pre-Alpine foliation. Gieré et al.
537 (2011) reported very similar garnet and tourmaline textures with a Ca-rich annulus
538 separating cores and rims from metapelites from the same area. As the protolith was
539 assumed to be a Permo-Carboniferous sediment (and thus would have experienced only
540 Alpine metamorphism), they interpreted that the annulus was formed during Alpine

541 prograde metamorphism at the transition from allanite to monazite. This is inconsistent
542 with the new age data that shows that the rocks around Laghetto di Campolungo belong
543 to the polymetamorphic basement of the Simano nappe and that no new monazite was
544 formed by the Alpine metamorphic cycle. Indeed, the reported trace element
545 compositions of monazite reported by Gieré et al. (2011) include 1200 ppm Pb, 42000
546 ppm Th and 5100 ppm U. The high amount of Pb is consistent with a Variscan age of the
547 monazite rather than an Alpine age (that would result in at least an order of magnitude
548 lower Pb content). Peak metamorphic temperatures for the Campolungo area have been
549 constrained between 600 and 625°C based on multi-phase equilibria (Fig. 1; Todd and
550 Engi 1997). On the other hand, Gieré et al. (2011) proposed a significantly higher peak T
551 of 660°C concomitant with small amounts of partial melting. Partial melting is well
552 known to enhance the recrystallization of monazite (Rubatto et al., 2001; Kelsey et al.,
553 2008). The absence of leucosomes in the field and the lack of Alpine age monazite in
554 these rocks are in better agreement with the lower peak metamorphic temperatures
555 proposed by Todd and Engi (1997).

556 Early Alpine dates around 33-34 Ma were obtained from the two fractions of Alpe
557 Sponda rutiles. In this sample, rutile is included both in large garnet grains (Grt I, II) and
558 small garnet grains (Grt III). Zr-in-rutile thermometry returns ~ 550 °C for all Sp9712
559 rutile grains analysed (most likely including both > 50 Ma and 33-34 Ma rutile), which is
560 significantly lower than the expected T_{\max} for this area (~620 °C, Todd and Engi, 1997).
561 This age has to be taken with caution, due to potential mixing with inherited
562 components, but it is possible, and in line with allanite data, that 33-34 Ma rutile formed
563 during a prograde stage at temperatures of ~ 550 °C.

564 The Alpine ages in the Campolungo area are constrained by accessory phases
565 found in the metamorphosed Permo-Mesozoic sedimentary rocks. Allanite in the
566 calcschist CLB-3 (31.7 ± 1.1 Ma) is included in Grt I and is aligned along the relic fabric
567 preserved in garnet (S1, Fig. 2c); garnet grains are wrapped and rotated by the
568 dominant foliation (S2). The allanite age is therefore interpreted to date prograde garnet
569 growth as well as the relic foliation along which the allanite is aligned. The dominant
570 foliation in this sample (S2) is correlated with the regional D2 (Grujic and Mancktelow,
571 1996; Maxelon and Mancktelow, 2005), the major deformation phase that refolded the
572 nappe stack and is responsible for many of the major tectonic structures in the
573 Lepontine dome. The relic foliation that is only preserved in garnet is likely to be S1,
574 and the allanite age (31.7 ± 1.1 Ma) may reflect the timing of the regional D1 nappe
575 stacking (Maxelon and Mancktelow, 2005). The HREE patterns in CLB-3 allanite cores
576 are depleted (Fig. 5b), providing evidence that allanite cores grew during/after prograde
577 garnet formation, which sequestered Mn and HREE.

578 Allanite in Campolungo quartzite Ma0901 (28.5 ± 1.3 Ma) is aligned along the
579 dominant foliation of the rock, which is likely to be a composite S1/S2 fabric (S1 and S2
580 are approximately parallel; e.g. Maxelon and Mancktelow, 2005). Rutile is included in
581 Ma0901 allanite cores and Zr-in-rutile thermometry indicates a temperature of ~
582 575 °C, which is below the estimated temperature for T_{max} conditions (600-625°C, Todd
583 and Engi, 1997). The allanite age is therefore interpreted to date a stage in the prograde
584 history of the rock during major tectonic reworking of the nappe pile (D2, Grujic and
585 Mancktelow, 1996; Maxelon and Mancktelow, 2005). Although garnet is not abundant in
586 the sample, the HREE depletion of allanite provides evidence that garnet was present at
587 the time of allanite formation (Fig. 5c).

588 The presence of relic igneous allanite in the Forcola orthogneisses and the Robiei
589 gneiss Ba0901 (the bulk composition of which is similar to orthogneiss, Table A1)
590 indicates that, in these samples, igneous allanite is the precursor to metamorphic
591 allanite. In the Robiei gneiss (Ba0901), metamorphic allanite cores (26.8 ± 1.3 Ma)
592 formed during prograde metamorphism and contain inclusions of biotite and muscovite.
593 Allanite domains in this sample show only a small decrease in total REE concentration
594 from cores through mantles and rims. It is speculated that allanite rims (19.7 ± 1.3 Ma)
595 formed by resorption whereby the allanite was partially consumed and recrystallised as
596 LREE allanite rims near T_{\max} conditions. This resorption likely occurred with very little
597 volume change (i.e. REE in allanite were neither concentrated nor diluted during
598 resorption). In this sample K-feldspar and plagioclase are fresh, indicating minimal fluid
599 influx during retrogression.

600 Rutile from Robiei calcschist (Ba0903A; Bündnerschiefer) returns TIMS dates that
601 span from 27 to 21 Ma – almost the entire range of allanite and monazite ages in the
602 western samples. Zr-in-rutile thermometry indicates that rutile crystallised over a
603 limited temperature range from 565 to 595 °C. The Zr-in-rutile temperatures overlap
604 with the expected T_{\max} for this area, based on multiphase equilibria thermobarometry
605 (Figure 1; Todd and Engi, 1997). Galli et al. (2007) investigated in detail the structures
606 and metamorphism of Bündnerschiefer in the Naret region, which is situated 5 km to the
607 northeast of Robiei. They proposed that main recrystallization of minerals (including
608 rutile) occurred between D2 and D3 and T_{\max} of 650 °C. The range of rutile dates is
609 consistent with either several episodes of rutile recrystallization during the D1-D3
610 deformation events or partial Pb loss from an early (>27 Ma) rutile generation formed
611 during prograde metamorphism.

612 Forcola orthogneiss allanite (scattering dates 25-32 Ma) is aligned along S1, a
613 dominant and early foliation. However, the timing of allanite crystallisation with respect
614 to metamorphic phase and deformation history is complicated by the large variety of
615 internal textures of allanite (Fig. 3f-h). The mosaic allanite from LEP0980 has a unique
616 texture of subgrain cores and rims, which reflect two allanite growth stages that
617 occurred at 31.3 ± 1.1 Ma for the cores and younger in the rims. Analyses from the
618 regularly zoned allanite from the same sample do not define an isochron age and single
619 spot dates span the entire range of mosaic allanite ages (25-32 Ma). There is no
620 correlation between the age of regularly zoned allanite and internal texture (i.e. core vs.
621 rim). It is possible that the older dates are the result of Pb inherited from a precursor
622 phase (Romer and Siegesmund, 2003), and thus these ages are not further considered in
623 the discussion. In allanite from sample LEP0807 there is no correlation between Th-Pb
624 age and internal texture (core vs. rim) and all analyses defined a Th-isochron age of 27.4
625 ± 0.6 Ma suggesting that any difference in age between allanite core and rim is below the
626 resolution of the analyses.

627 Croveo schist (Ma9330) monazite age of 21.7 ± 0.3 Ma is interpreted to date the
628 timing of monazite crystallisation at the expense of allanite. Allanite as a precursor to
629 monazite (see also Romer and Siegesmund, 2003; Janots et al., 2008) is inferred from
630 the presence of relic allanite included in garnet. The HREE pattern of monazite is
631 depleted with respect to the bulk rock, suggesting that garnet was still stable when
632 monazite was forming (Fig. 5h). Additionally, the negative Eu anomaly is more
633 pronounced in monazite than in the bulk rock and thus plagioclase was also stable. As
634 garnet and plagioclase are peak metamorphic minerals, it is reasonable to assume that
635 monazite formed close to T_{\max} conditions of 620°C at 6.2 kbar (Todd and Engi, 1997).

636 The paragneisses of Alpe Sponda belong to the basement of the Simano nappe and
637 thus it is plausible that these samples underwent polymetamorphism as is the case for
638 the Campolungo metapelites (see above). Element maps as well as trace element profiles
639 through the large garnet grains suggest that Grt I has been resorbed prior to the
640 formation of Grt II rims and newly formed Grt III. This is very similar to the two
641 generations of garnet found in sample CLM-6, where a pre-Alpine garnet core is
642 truncated by an Alpine rim. Two distinct types of garnet with the same compositional
643 characteristics as in our study (Fig. 4g-h) have been reported by Beitter et al. (2008)
644 from the Alpe Sponda area. Beitter et al. (2008) report garnet grains corresponding to
645 Grt I were only found in the paragneiss whereas grains corresponding to Grt III were
646 associated to the Alpine rutile-kyanite-quartz veins.

647 Allanite is a precursor to monazite in Alpe Sponda fels Sp9712. Rare allanite has
648 been observed in the garnet whereas no monazite is observed as inclusions in garnet.
649 The assembly of small monazite grains that satellite relic allanite (Fig. 3e) also indicates
650 that monazite replaced allanite in these rocks. The Alpe Sponda fels monazite (22.0 ± 0.3
651 Ma) returned the youngest ages of the Central samples. The steady increase of Dy/Lu
652 and an associated increase of the negative Eu anomaly (Fig. 5h) suggest that this
653 monazite formed together with garnet and plagioclase, the peak assemblage. Thus, we
654 conclude that peak metamorphic conditions persisted up to 22 Ma in this area.

655 Campolungo calcschist (CLB-4) returned rutile dates between 19-25 Ma. Rutile
656 crystallised after garnet (one of the earliest prograde minerals preserved) and before
657 staurolite (one of the later-stage minerals). The Zr-in-rutile temperature for CLB-4 is ~
658 625 °C, similar to the estimate for maximum Barrovian temperature conditions in this
659 area (600-620 °C; Todd and Engi, 1997). The spread of rutile dates may again reflect

660 protracted rutile crystallisation during slow heating while temperatures approached
661 T_{\max} and/or cooling ages.

662 *7.3. Implications for the allanite-to-monazite transition in metamorphic rocks*

663 Our regional scale data set provides an excellent framework to shed light on the
664 nature of the allanite-to-monazite transition during Barrovian metamorphism (Fig. 9).
665 Rutile inclusions in allanite from Campolungo Ma0901 quartzite provide evidence that
666 the crystallisation of allanite cores occurred at a temperature of ~ 575 °C, as determined
667 by Zr-in-rutile thermometry of rutile inclusions. Moreover, the similarity of the allanite
668 ages from the calcschist and quartzite (~ 32 Ma and ~ 28 Ma respectively) and their
669 textural positions associated with the amphibolite-facies S1 and S2 foliation, indicates
670 that allanite crystallisation in the calcschist did not occur at the low temperatures of
671 400-450 °C suggested by previous studies of prograde allanite (e.g. Smith and Berreiro,
672 1990; Wing et al., 2003; Janots et al., 2008; Rasmussen and Muhling, 2009; Janots et al.,
673 2011).

674 Robiei gneiss (Ba0901) allanite is an example of two separate phases of allanite
675 crystallisation in the same rock under different conditions. Allanite prevails in this rock,
676 which contains very little Ca (0.74 %), and has a low Ca/Al ratio of 0.08. At the
677 metamorphic conditions attained and for a rock of this bulk composition, the models of
678 both Spear (2010) and Wing et al. (2003) predict monazite stability (Fig. 9). It is inferred
679 that allanite rims crystallised (instead of monazite) at the expense of allanite because
680 T_{\max} was too low for monazite stability in this sample ($T_{\max} \sim 575$ °C).

681 Monazite crystallisation in samples Ma9330 and Sp9712 is interpreted to have
682 occurred close to T_{\max} conditions (~ 620 °C). This is somewhat higher than the reaction
683 temperatures suggested by previous studies of natural samples (560-580 °C in Janots et

684 al., 2008; ~ 540 °C in Gieré et al., 2011) and in thermodynamic models (Spear 2010).
685 The model of Spear (2010) proposes a temperature range of 400 to 700 °C for the
686 allanite-to-monazite reaction, depending on bulk Ca, Al and pressure (Fig. 9a,b). For bulk
687 composition of sample Ma9330 (Table A1) the model predicts that the allanite-to-
688 monazite reaction would occur at ~ 450 °C (P = 5 kbar); at 10 kbar the reaction is
689 predicted to occur at ~ 500 °C. However the model assumes simple systems and the
690 studied samples are more complex; neither of the reaction temperature predictions is
691 consistent with our observations. Furthermore, the model predicts that the reaction
692 would have occurred even in samples where allanite is the stable REE mineral (Fig.
693 9a,b). Spear and Pyle (2010) admit that good thermodynamic data for allanite is lacking
694 and the disagreement between observations in this study and predicted reaction
695 temperatures may be due to the thermodynamic data used. One of the major limitations
696 in applying thermodynamic models to accessory mineral reactions is the difficulty in
697 defining the reactive bulk composition. Particularly for minerals whose stabilities are
698 controlled by trace elements, their reactive bulk is likely not equivalent to the rock
699 composition and local difference in trace element distributions will have major
700 consequences on accessory mineral reactions. Additionally, deformation and partial
701 hydration may localize reactions. The survival of Carboniferous monazite in
702 Campolungo samples CLM-5 and 6 provides evidence that in these basement samples no
703 Alpine prograde allanite formed. This might be related to a limited
704 retrogression/hydration of these amphibolite-facies schists postdating the Variscan
705 orogeny. In contrast, Alpe Sponda sample Sp9712 contains exclusively Alpine monazite
706 that has relic allanite included, indicating an Alpine prograde growth of monazite from
707 allanite.

708 It has been proposed that bulk composition (especially Ca concentration and Ca/Al
709 ratio) plays a key role for the allanite to monazite transition (Wing et al., 2003). This
710 effect may explain allanite stabilisation at lower T in the calcschist than in the quartzite,
711 but this model only holds for the Campolungo samples. CaO contents and Ca/Al ratio do
712 not account for allanite's perpetuation or its replacement by monazite in all samples.
713 The monazite- and allanite- stable areas in Ca/Al space proposed by Wing et al. (2003)
714 do not hold for Central Alps samples studied here (Fig. 9c) and by Janots et al. (2008,
715 2011). This is a strong indication that the reactive bulk composition may play a
716 significant role in accessory mineral stability.

717 The inconsistencies between conclusions reached from the study of natural
718 samples and those from thermodynamic models show that not enough is known about
719 the factors governing allanite and monazite stability to predict the conditions of allanite-
720 in and monazite-in reactions in pelitic to granitic compositions. This reinforces the need
721 for sample-specific petrological considerations (e.g. textural relationships, deformation,
722 effective reactive bulk) in order to link accessory mineral ages with metamorphism.

723 *7.4. Trend of ages across the Lepontine dome*

724 A regional pattern for Barrovian metamorphism develops when the histories of the
725 Croveo-Robiei and Campolungo-Sponda samples are combined with studies from the
726 literature (Fig. 10). Excluding ages from the Southern Steep Belt (SSB), crystallisation
727 ages fall into two groups: older ages (27 to 33 Ma) are interpreted as prograde ages that
728 relate to major, orogen-scale tectonic movements (nappe stacking) and younger ages
729 that can be linked to post-collisional mineral growth close to T_{\max} . Prograde allanite ages
730 are in good agreement with the 29-32 Ma Th-Pb allanite ages of Janots et al. (2009) and

731 a greenschist-facies K-Ar amphibole age of 29 ± 3 Ma (Deutsch and Steiger, 1985), both
732 from the Northern Steep Belt (NSB).

733 U-Pb garnet ages of Vance and O’Nions (1992) from the NSB also agree with
734 prograde allanite ages from this study. The garnet investigated by Vance and O’Nions
735 (1992) are re-interpreted as prograde based on the petrological relationships described
736 in that study (i.e. garnet is pre- to synkinematic with the dominant foliation), which are
737 similar to petrological relationships of samples from the current study, in which garnet
738 is a prograde phase.

739 These prograde ages in the northern part of the Lepontine belt coincide with the
740 age of post-HP greenschist-facies overprint dated in Valaisan units in the northeastern
741 Lepontine (Wiederkehr et al., 2009). In the north, progressive regional metamorphism
742 thus reached greenschist-facies conditions within 2-10 Ma after HP metamorphism in
743 the Valaisan units (Wiederkehr et al., 2009), and in Cima Lunga and Adula melange units
744 (Fig. 10, Becker, 1993; Gebauer, 1996; Brouwer et al., 2005; Hermann et al., 2006; Liati
745 et al., 2009). However, the Valaisan units showing HP metamorphism, as well as the
746 *mélange* units, were exhumed prior to their Barrovian overprint, which postdates
747 nappe emplacement. The correlation of allanite ages with dominant deformation
748 structures suggests that the main deformation event occurred during this time interval,
749 i.e. 32-27 Ma (“stage 2” of Berger et al., 2011); isoclinal refolding of the nappes probably
750 initiated during the later part of this phase. The resolution of ages is not sufficient to
751 evaluate whether there is an E-W age progression in the nappe stacking phase, but a S-N
752 younging of the main deformational phases has been previously established (Berger et
753 al., 2011).

754 The thermal peak followed nappe stacking and maximum ages for this stage are
755 recorded by monazite and a minimum age by Ba0901 allanite rims (Fig. 10). Isograds
756 are clearly discordant to the structures established during the nappe stacking events,
757 providing evidence on a regional scale that thermal metamorphism outlasted this
758 deformation event (Fig. 11a). The regional scale, south-west verging, ductile transverse
759 folding (F4 of Steck et al., 2013) likely occurred close to T_{\max} . Combining formation ages
760 that likely record a stage close to maximum T from this study with well-constrained ages
761 from the literature, especially additional monazite ages from further south (Köppel and
762 Grünenfelder, 1975) reveals a consistent trend with metamorphic grade (Fig. 11b). As
763 outlined by the dashed line, younger ages (18-20 Ma) are found in the lower grade rocks
764 ($T_{\max} = 550\text{-}580^{\circ}\text{C}$) of the north, and older ages (21-23 Ma) occur in the higher grade
765 rocks ($T_{\max} = 590\text{-}650^{\circ}\text{C}$) towards the middle and southern part of the Barrovian
766 sequence.

767 The general trend for crystallisation ages does not apply to rocks of the SSB. Ages
768 for the SSB migmatisation span the entire age range of prograde and T_{\max} ages from the
769 subsolidus rocks (Figs. 11 and 12). The spread of ages from 22 to 32 Ma for migmatites
770 has been interpreted to reflect an extended period of upper-amphibolite facies
771 metamorphism with protracted incipient melting during various deformation stages in
772 the SSB (Rubatto et al., 2009; Gregory et al., 2012). Partial melting persisted to 22 Ma,
773 indicating that the rocks resided above the wet solidus ($T \geq 650^{\circ}\text{C}$). It should be noted
774 that fission track data (Hurford 1986) show ages around 19 Ma for the partial annealing
775 of zircon in samples from the SSB, reflecting cooling rates $>100^{\circ}\text{C}/\text{Ma}$ for that part of
776 the Lepontine dome.

777 The emerging picture for the age of Barrovian metamorphism for the Lepontine
778 dome is that high temperatures in the southern and central areas lasted to 21-23 Ma,
779 whereas in the north-western part they are slightly younger with ages of 18-20 Ma. The
780 combined age data for main deformations and T_{\max} thus suggest that, at least in the
781 central and southern Lepontine, amphibolite-facies conditions were retained for up to
782 10 Ma after nappe stacking, allowing for multiple phases of ductile deformation (Steck et
783 al., 2013). At ~20 Ma, late-orogenic shortening and uplift was accommodated by intense
784 phases of folding, associated with backthrusting in the south, thus producing the two
785 steep belts (SSB and NSB; Berger et al., 2011).

786 Ages of Hurford (1986) and Steck and Hunziker (1994) suggest that rocks of the
787 Croveo-Robiei area had cooled below retention of Rb-Sr in biotite (~ 300 °C) by ~15 Ma
788 and below ~250 °C by ~ 12-15 Ma (zircon fission track). Hurford (1986) also reports a
789 Rb/Sr muscovite age of ~ 18 Ma ($T \approx 500$ °C, Hurford, 1986) for samples to the East of
790 Ma9330 (Fig. 10b). Similarly, rapid cooling to below ~ 250 °C by 10-13 Ma is
791 documented for the Campolungo-Sponda area (Hurford, 1986; Janots et al., 2009; Fig.
792 10). Therefore, the Central and Northern part of the Lepontine dome must have
793 experienced very rapid cooling after ~20 Ma.

794 Insight into the cooling history of the eastern samples is provided by Ar-Ar white
795 mica ages from the same samples, as well as one sample from the hanging wall of the
796 Forcola fault (which contain no Alpine allanite). White mica from the hanging wall and
797 footwall of the Forcola fault return Ar-Ar ages of 27-25 Ma and 22-21 Ma respectively
798 (Augenstein, 2013). The younger age in the footwall is interpreted to reflect the onset of
799 grain size reduction and mylonitisation along the Forcola fault (Augenstein, 2013). The
800 Ar-Ar ages also suggest that temperatures were below Ar retention in white mica at 22-

801 21 Ma for the Forcola rocks. K-Ar ages of biotite in this area are around 20 Ma (Steck and
802 Hunziker, 1994) and provide further evidence for rapid cooling. In an east-west
803 traverse, the K-Ar ages of biotite are progressively younger towards the west, suggesting
804 that cooling propagated from east to west (Steck et al., 2013).

805 The accelerated cooling at about 20 Ma, observed throughout the Lepontine dome,
806 did not result in an increased sedimentation rate as would be expected if cooling was a
807 result of increased uplift, erosion and associated exhumation. In contrast, the detailed
808 study of the stratigraphy in the foreland basins surrounding the Lepontine dome reveals
809 that erosion rates decreased by about 50 % at 20 Ma (Schlunegger, 1999). Therefore, the
810 fast cooling around 20 Ma is likely related to exhumation of the Central Alps during a
811 phase of transtensional tectonics (Ciancaleoni and Marquer, 2008). This exhumation
812 might have been accommodated by nearly simultaneous top-to-the-West normal
813 faulting along the Simplon normal fault (Mancktelow, 1992), vertical displacement
814 during back thrusting along the Insubric Line (Schmid et al., 1989) and perhaps normal
815 fault movement on the Forcola line (Ciancaleoni and Marquer, 2008). In any case, the
816 tight age constraints for the transition from low-grade metamorphism to amphibolite-
817 facies conditions across the Central Alps (Figs. 11, 12) provide powerful constraints for
818 the interpretation of this classical orogeny.

819

820 **Acknowledgements**

821 The authors acknowledge the technical assistance of Robert Rapp for EMP analysis,
822 Charlotte Allens for LA-ICP-MS analysis and Peter Holden for SHRIMP analysis.
823 Fernando Corfu is thanked for comments on a previous version of the manuscript.
824 Constructive comments from Antonio Langone and an anonymous reviewer and
825 editorial handling by M. Scambelluri are acknowledged.

826 **Table captions**

827 **Table 1:** Sample overview showing the main and accessory mineral assemblage, the
828 minerals used for dating and the results of U-Th-Pb geochronology.

829

830

831 **Figure captions**

832 **Figure 1:** (a) Tectonic overview of the Central Alps and sample locations (after
833 Trommsdorf et al., 2000; Berger et al., 2005; Burri et al., 2005; Maxelon and Mancktelow,
834 2005; Janots et al., 2008). (b) Central Alps map with isotherms for Barrovian
835 metamorphism that overprinted the major tectonic boundaries (Todd and Engi, 1997)
836 and sample numbers. Swiss grid coordinates are in kilometres. For a colour version of
837 the Figure please refer to the online version of the article.

838 **Figure 2:** Photomicrographs of (a) Ma9330 S2 white micas and biotite wrapping
839 garnet (note that S1 and S2 are sub-parallel in these samples); (b) CLB-3 garnet, which
840 preserves internal S1 fabric, rotated and wrapped by S2 white mica and biotite; (c)
841 Monazite crystal in CLM-6 that is aligned along the main foliation defined by micas and
842 graphite; (d) Ma0901 allanite aligned along the S1/S2 fabric; (e) Sp9712 large staurolite
843 crystals surrounding kyanite that is partially replaced by white mica; (f) LEP0980
844 allanite aligned along the dominant fabric (S1). A detailed petrographic description of
845 the samples is given in the electronic Appendix.

846 **Figure 3:** (a) Backscatter electron (BSE) image and (b) compositional map of
847 Ba0901 allanite showing an allanite rich-core (C), epidote mantle (M) and allanite rim
848 (R). BSE images of (c) CLB-3 allanite; (d) Ma0901 allanite, arrows point to rutile
849 inclusions in the allanite core; (e) Sp9712 monazite satellites of a relic allanite; (f)

850 LEP0979 allanite rims on epidote-rich cores; (g) LEP0807 allanite; (h) LEP0980 mosaic
851 allanite and regularly zoned allanite (P = pre-Alpine relics).

852 **Figure 4:** Garnet composition (data from Table A2). Ma9330 garnet: (a) MgO,
853 MnO and Lu profile across the garnet; O. Rim = outer rim of the garnet; (b) chondrite-
854 normalised REE, the systematic depletion in HREE from core (C) to rim (R) is indicated
855 by the arrow; outer rim garnet is mildly enriched in MREE. (c) MgO, MnO and Lu profile
856 across CLB-3 garnet, showing a sharp increase in Lu from Grt I rim to Grt II; (d)
857 chondrite-normalised REE patterns of CLB-3 garnet. (e) MgO, MnO and CaO profile
858 across CLM-6 garnet. The co-rim boundaries (vertical dashed lines) are based on the
859 element map shown in (f). (f) element distribution map of Ca in garnet from CLM-6. Note
860 the Alpine rim cutting across the regular zoning in the pre-Alpine core. (g) LA ICPMS
861 profile across Sp9712 Grt I and II; location of the profile is given in the Ca map (inset). I_c,
862 I_r = Grt I core and rim respectively, II_c = Grt II core etc. (f) Sp9712 chondrite-normalised
863 REE patterns of garnets I-III. Inset shows Ca map of Grt III. The decrease in HREE from
864 core to rim is indicated.

865 **Figure 5:** Chondrite-normalised REE composition of accessory allanite (a-f) and
866 monazite (g-h) compared with whole rock (WR). REE of allanite cores, mantles and rims
867 of (a) Ba0901, (b) CLB-3 and (c) Ma0901. (d) A comparison of allanite growth zones in
868 terms of REE and Th/U in metasediments. REE of allanite in Forcola orthogneiss
869 samples (e) LEP0807 and LEP0979 and (f) LEP0980. (g) REE of monazite in Croveo
870 schist (Ma9330) and Alpe Sponda fels (Sp9712). (h) REE compositional variation in
871 Alpine monazite. The effect of feldspar and garnet coexistence is indicated with arrows.

872 **Figure 6:** Summary of geochronology results grouped by area (Western, Central
873 and Eastern Lepontine) and by phase dated. Monazite and allanite ages are formation
874 ages, whereas rutile dates are more difficult to interpret, see text for discussion.

875 **Figure 7:** Monazite ages. (a) Concordia plot for monazite analyses in samples CLM-
876 5 and CLM-6 (a), in sample Ma9330 (b) and in sample Sp9712. Average $^{206}\text{Pb}/^{238}\text{U}$ ages
877 are given in (a), concordia ages are given in (b) and (c) and are represented by the blue
878 ellipses. The unfilled ellipses in (a) and (c) are not used for age calculation. A
879 representative BSE image of dated monazite is shown on the right of plot (a) and (c).

880 **Figure 8:** Allanite Th-Pb isochrons for (a) Ba0901 allanite cores; (b) Ba0901
881 allanite rims; (c) CLB-3 allanite cores; (d) Ma0901 allanite cores; (e) LEP0980 mosaic
882 allanite cores; (f) LEP0807 allanite (cores and rims). The model common Pb
883 composition (Stacey and Kramers, 1975) is indicated on the y-axis and always close to
884 the intercept defined by the isochron. Error ellipses are 2σ ; errors quoted on isochron
885 ages are 95 % confidence.

886 **Figure 9:** Allanite- and monazite-bearing samples of Alpine age compared to
887 modelled stability fields. (a) Samples plotted in terms of temperature and bulk-rock CaO
888 with stability fields calculated by Spear (2010). Numbers next to symbols are wt %
889 Al_2O_3 . Reaction lines of Spear (2010) were calculated for 5 kbar pressure; the reaction is
890 predicted to occur at higher temperature with increasing bulk CaO, and the slope is
891 dependent on bulk Al_2O_3 . (b) Samples plotted in the allanite-monazite P-T stability field
892 of Spear (2010). Numbers indicate the sample whole rock CaO concentration (wt %);
893 more than one number next to a symbol indicates more than one sample from the same
894 locality. Two reaction curves are plotted: one for low CaO and one for moderate Ca
895 concentration. (c) $\text{Al}/\text{Al}_{\text{Shaw}}$ vs. $\text{Ca}/\text{Ca}_{\text{Shaw}}$, where Al_{Shaw} and Ca_{Shaw} are concentrations for

896 an "average pelite" (Shaw, 1956). The discrimination line of Wing et al. (2003) shows
897 the expected stability of allanite and monazite for metapelites in andalusite, kyanite and
898 sillimanite zones. None of the diagrams predicts correctly the allanite or monazite
899 presence in the studied samples.

900 **Figure 10:** Summary of Alpine metamorphism in the Central Alps. (a) An overview
901 of interpretation of metamorphic ages in the Lepontine Alps; (b) Temperature-time
902 paths for samples studied as well as for the Southern Steep Belt (SSB), Northern Steep
903 Belt (NSB) and the Urseren zone, taken from the literature as indicated. (1) Becker,
904 1993; (2) Gebauer, 1996; (3) Brouwer et al., 2005; (4) Wiederkehr et al., 2009; (5)
905 Deutsch and Steiger, 1985; (6) Janots et al., 2009; (7) Vance and O'Nions, 1992; (8)
906 Janots and Rubatto, 2014; (9) Köppel and Grünenfelder, 1975; (10) Hurford, 1986; (11)
907 Liati et al., 2000; (12) von Blanckenburg, 1992; (13) Oberli et al., 2004; (14) Gregory et
908 al., 2012; (15) Rubatto et al., 2009; (16) Augenstein, 2013.

909 **Figure 11:** Trend of ages across the Lepontine dome. (a) Map of isotherms with
910 locations of samples included in (b). Note that the study site of Janots and Rubatto
911 (2014) is north of the map area. (b) Metamorphic grade (T_{\max}) vs. allanite, monazite and
912 zircon crystallisation age from this and selected studies from the literature as indicated.
913 Legend is the same for both (a) and (b).

914

915

916 **References**

- 917 Allaz, J., Engi, M., Berger, A., Villa, I.M., 2011. The effects of retrograde reactions and
918 of diffusion on ⁴⁰Ar-³⁹Ar ages of micas. *Journal of Petrology*, 52, 691-716.
- 919 Augenstein, C., 2013. The formation of the Lepontine gneiss dome. Ph.D.
920 dissertation, Australian National University, Canberra, Australia.
- 921 Becker, H., 1993. Garnet peridotite and eclogite Sm-Nd mineral ages from the
922 Lepontine dome (Swiss Alps): New evidence for Eocene high-pressure metamorphism in
923 the central Alps. *Geology*, 21, 599-602.
- 924 Beitter, T., Wagner, T., Markl, G., 2008. Formation of kyanite-quartz veins of the
925 Alpe Sponda, Central Alps, Switzerland: implications for Al transport during regional
926 metamorphism. *Contributions to Mineralogy and Petrology*, 156, 689-707.
- 927 Berger, A., Mercolli, I., Engi, M., 2005. The central Lepontine Alps: Notes
928 accompanying the tectonic and petrographic map sheet Sopra Ceneri (1:100'000).
929 *Schweizerische Mineralogische und Petrographische Mitteilungen*, 85, 109-146.
- 930 Berger, A., Schmid, S.M., Engi, M., Bousquet, R., Wiederkehr, M., 2011. Mechanisms
931 of mass and heat transport during Barrovian metamorphism: A discussion based on field
932 evidence from the Central Alps (Switzerland/northern Italy). *Tectonics*, 30, TC1007.
- 933 Brouwer, F.M., Burri, T., Engi, M., Berger, A., 2005. Eclogite relics in the Central
934 Alps: PT - evolution, Lu-Hf ages and implications for formation of tectonic mélange
935 zones. *Schweizerische Mineralogische und Petrographische Mitteilungen*, 85, 147-174.
- 936 Brouwer, F.M., van de Zedde, D.M.A., Wortel, M.J.R., Vissers, R.L.M., 2004. Late-
937 orogenic heating during exhumation: Alpine PTt trajectories and thermomechanical
938 models. *Earth and Planetary Science Letters*, 220, 185-199.
- 939 Budzyn, B., Hetherington, C.J., Williams, M.L., Jercinovic, M.J., Michalik, M., 2010.
940 Fluid-mineral interactions and constraints on monazite alteration during
941 metamorphism. *Mineralogical Magazine*, 74, 659-681.
- 942 Buick, I.S., Hermann, J., Williams, I.S., Gibson, R., Rubatto, D., 2006. A SHRIMP U-Pb
943 and LA-ICP-MS trace element study of the petrogenesis of garnet-cordierite-
944 orthoamphibole gneisses from the Central Zone of the Limpopo Belt, South Africa.
945 *Lithos*, 88, 150-172.

946 Burri, T., Berger, A., Engi, M., 2005. Tertiary migmatites in the Central Alps:
947 Regional distribution, field relations, conditions of formation, and tectonic implications.
948 Schweizerische Mineralogische und Petrographische Mitteilungen, 85, 215-232.

949 Ciancaleoni, L., Marquer, D., 2008. Late Oligocene to early Miocene lateral extrusion
950 at the eastern border of the Lepontine Dome of the Central Alps (Bergell and Insubric
951 areas, eastern Central Alps). Tectonics, 27, TC4008.

952 Cherniak, D.J., 2000. Pb diffusion in rutile. Contributions to Mineralogy and
953 Petrology 139, 198-207.

954 Deutsch, A., Steiger, R.H., 1985. Hornblende K-Ar ages and the climax of Tertiary
955 metamorphism in the Lepontine Alps (south-central Switzerland) an old problem
956 reassessed. Earth and Planetary Science Letters, 72, 175-189.

957 Engi, M., 2017. Petrochronology based on REE-minerals: Monazite, allanite,
958 xenotime, apatite. Reviews in Mineralogy and Geochemistry 83, in press.

959 Engi, M., Todd, C.S., Schmatz, D., 1995. Tertiary metamorphic conditions in the
960 eastern Lepontine Alps. Schweizerische Mineralogische und Petrographische
961 Mitteilungen, 75, 347-396.

962 Ewing T.A., Hermann, J., Rubatto, D., 2013. The robustness of the Zr-in-rutile and
963 Ti-in-zircon thermometers during high-temperature metamorphism (Ivrea-Verbano
964 Zone, northern Italy). Contributions to Mineralogy and Petrology, 165, 757-779.

965 Ferry, J.M., Watson, E.B., 2007. New thermodynamic models and revised
966 calibrations for the Ti-in-zircon and Zr-in-rutile thermometers. Contributions to
967 Mineralogy and Petrology, 154, 429-437.

968 Finger, F., Broska, I., Roberts, M.P., Schermaier, A., 1998. Replacement of primary
969 monazite by apatite-allanite-epidote coronas in an amphibolite facies granite gneiss
970 from the eastern Alps. American Mineralogist, 83, 248-258.

971 Foster, G., Gibson, H.D., Parrish, R., Horstwood, M., Fraser, J., Tindle, A., 2002.
972 Textural, chemical and isotopic insights into the nature and behaviour of metamorphic
973 monazite. Chemical Geology, 191, 183-207.

974 Frey, M., Bucher, K., Frank, E., Mullis, J., 1980. Alpine metamorphism along the
975 Geotraverse Basel-Chiasso – a review. Eclogae Geologicae Helvetiae, 73, 527-546.

976 Frey, M., Hunziker, J.C., Frank, W., Bocquet, J., Dal Piaz, G.V., Jäger, E., Niggli, E.,
977 1974. Alpine metamorphism in the Alps: A review. *Schweizerische Mineralogische und*
978 *Petrographische Mitteilungen*, 54, 247-290.

979 Galli, A., Mancktelow, N., Reusser, E., Caddick, M., 2007. Structural geology and
980 petrography of the Naret region (northern Valle Maggia, N.Ticino, Switzerland). *Swiss*
981 *Journal of Geosciences*, 100, 53-70.

982 Garofalo, P.S., 2012. The composition of Alpine marine sediments
983 (Bündnerschiefer Formation, W Alps) and the mobility of their chemical components
984 during orogenic metamorphism. *Lithos*, 128-131, 55-72.

985 Gebauer, D., 1996. A P-T-t Path for an (ultra?-) high-pressure ultramafic/mafic
986 rock-association and its felsic country-rocks based on SHRIMP-dating of magmatic and
987 metamorphic zircon domains. Example: Alpe Arami (Central Swizz Alps). In A. Basu, and
988 S. Hart (Eds.), *Earth processes: Reading the isotopic code*, American Geophysical Union
989 *Monograph 95*, pp. 307-329.

990 Gieré, R., Rumble, D., Günther, D., Connolly, J., Caddick, M.J., 2011. Correlation of
991 growth and breakdown of major and accessory minerals in metapelites from
992 Campolungo, Central Alps. *Journal of Petrology*, 52, 2293-2334.

993 Gregory, C.J., Rubatto, D., Allen, C.M., Williams, I.S., Hermann, J., Ireland, T., 2007.
994 Allanite micro-geochronology: A LA-ICP-MS and SHRIMP U-Th-Pb study. *Chemical*
995 *Geology*, 245, 162-182.

996 Gregory, C.J., Rubatto, D., Hermann, J., Berger, A., Engi, M., 2012. Allanite behaviour
997 during incipient melting in the southern Central Alps. *Geochimica et Cosmochimica Acta*,
998 84, 433-458.

999 Grujic, D., Mancktelow, N.S., 1996. Structure of the northern Maggia and Lebendun
1000 Nappes, Central Alps, Switzerland. *Eclogae Geologicae Helvetiae*, 89, 461-504.

1001 Hermann, J., Rubatto, D., 2003. Relating zircon and monazite domains to garnet
1002 growth zones: age and duration of granulite facies metamorphism in the Val Malenco
1003 lower crust. *Journal of metamorphic Geology*, 21, 833-852.

1004 Hermann, J., Rubatto, D., Trommsdorff, V., 2006. Sub-solidus Oligocene zircon
1005 formation in garnet peridotite during fast decompression and fluid infiltration (Duria,
1006 Central Alps). *Mineralogy and Petrology*, 88, 181-206.

1007 Hunziker, J.C., 1969. Rb/Sr Altersbestimmungen aus den Walliser Alpen.
1008 Hellglimmer- und Gesamtgesteinsalterswerte. *Eclogae Geologicae Helvetiae*, 62, 527-
1009 542.

1010 Hurford, A.J., 1986. Cooling and uplift patterns in the Lepontine Alps South Central
1011 Switzerland and an age of vertical movement on the Insubric fault line. *Contributions to*
1012 *Mineralogy and Petrology*, 92, 413-427.

1013 Jäger, E., 1973. Die alpine Orogenese im Lichte der radiometrischen
1014 Altersbestimmung. *Eclogae Geologicae Helvetiae*, 66, 11-21.

1015 Janots, E., Berger, A., Engi, M., 2011. Physico-chemical control on the REE minerals
1016 in chloritoid-grade metasediments from a single outcrop (Central Alps, Switzerland).
1017 *Lithos*, 121, 1-11.

1018 Janots, E., Brunet, F., Goffé, B., Poinssot, C., Burchard, M., Cemič, L., 2007.
1019 Thermochemistry of monazite-(La) and dissakisite-(La): implications for monazite and
1020 allanite stability in metapelites. *Contributions to Mineralogy and Petrology*, 154, 1-14.

1021 Janots, E., Engi, M., Berger, A., Allaz, J., Schwartz, J.-O., Spandler, C., 2008. Prograde
1022 metamorphic sequence of REE minerals in pelitic rocks of the Central Alps: implications
1023 for allanite–monazite–xenotime phase relations from 250 to 610 °C. *Journal of*
1024 *metamorphic Geology*, 26, 509-526.

1025 Janots, E., Engi, M., Rubatto, D., Berger, A., Gregory, C., Rahn, M., 2009. Metamorphic
1026 rates in collisional orogeny from in situ allanite and monazite dating. *Geology*, 37, 11-14.

1027 Janots, E., Rubatto, D., 2014. U–Th–Pb dating of collision in the external Alpine
1028 domains (Urseren zone, Switzerland) using low temperature allanite and monazite.
1029 *Lithos*, 184-187, 155-166.

1030 Kelsey, D.E., Clark, C., Hand, M., 2008. Thermobarometric modelling of zircon and
1031 monazite growth in melt-bearing systems: examples using model metapelitic and
1032 metapsammitic granulites. *Journal of Metamorphic Geology*, 26, 199-212.

1033 Kim, Y., Yi, K., Cho, M., 2009. Parageneses and Th-U distributions among allanite,
1034 monazite, and xenotime in Barrovian-type metapelites, Imjingang belt, central Korea.
1035 *American Mineralogist*, 94, 430-438.

1036 Kooijman, E., Mezger, K., Berndt, J., 2010. Constraints on the U-Pb systematics of
1037 metamorphic rutile from in situ LA-ICP-MS analysis. *Earth and Planetary Science Letters*,
1038 293, 321-330.

1039 Köppel, V., Grünenfelder, M., 1975. Concordant U-Pb ages of monazite and
1040 xenotime from the Central Alps and the timing of high temperature Alpine
1041 metamorphism, a preliminary report. *Schweizerische Mineralogische und*
1042 *Petrographische Mitteilungen*, 55, 129-132.

1043 Liati, A., Gebauer, D., Fanning, C.M., 2000. U-Pb SHRIMP dating of zircon from the
1044 Novate granite (Bergell, Central Alps): evidence for Oligocene-Miocene magmatism,
1045 Jurassic/Cretaceous continental rifting and opening of the Valais trough. *Schweizerische*
1046 *Mineralogische und Petrographische Mitteilungen*, 80, 305-316.

1047 Liati, A., Gebauer, D., Fanning, C.M., 2009. Geochronological evolution of HP
1048 metamorphic rocks of the Adula nappe, Central Alps, in pre-Alpine and Alpine
1049 subduction cycles. *Journal of the Geological Society, London*, 166, 797-810.

1050 Mancktelow, N.S., 1992. Neogene lateral extension during convergence in the
1051 Central Alps: Evidence from interrelated faulting and backfolding around the
1052 Simplonpass (Switzerland). *Tectonophysics*, 215, 295-317.

1053 Maxelon, M., Mancktelow, N.S., 2005. Three-dimensional geometry and
1054 tectonostratigraphy of the Pennine zone, Central Alps, Switzerland and Northern Italy.
1055 *Earth Science Reviews*, 71, 171-227.

1056 Nagel, T., de Capitani, C., Frey, M., 2002. Isograd and P-T evolution in the eastern
1057 Lepontine Alps (Graubünden, Switzerland). *Journal of metamorphic Geology*, 20, 309-
1058 324.

1059 Niggli, E., Niggli, C.R., 1965. Karten der Verbreitung einiger Mineralien der
1060 alpidischen Metamorphose in den Schweizer Alpen (Stilpnomelan, Alkali-Amphibol,
1061 Chloritoid, Staurolith, Disthen, Sillimanit). *Eclogae Geologicae Helvetiae*, 58, 335-368.

1062 Oberli, F., Meier, M., Berger, A., Rosenberg, C., Gieré, R., 2004. U-Th-Pb and
1063 $^{230}\text{Th}/^{238}\text{U}$ disequilibrium isotope systematics: Precise accessory mineral chronology
1064 and melt evolution tracing in the Alpine Bergell intrusion. *Geochimica et Cosmochimica*
1065 *Acta*, 68, 2543-2560.

1066 Pollington, A.D., Baxter, E.F., 2010. High resolution Sm-Nd garnet geochronology
1067 reveals the uneven pace of tectonometamorphic processes. *Earth and Planetary Science*
1068 *Letters*, 293, 63-71.

1069 Rasmussen, B., Muhling, J.R., 2009. Reactions destroying detrital monazite in
1070 greenschist-facies sandstones from the Witwatersrand basin, South Africa. *Chemical*
1071 *Geology*, 264, 311-327.

1072 Regis, D., Rubatto, D., Darling, J., Cenki-Tok, B., Zucali, M., Engi, M., 2014. Multiple
1073 metamorphic stages within an eclogite-facies terrane (Sesia Zone, Western Alps)
1074 revealed by Th-U-Pb petrochronology. *Journal of Petrology*, 55, 1429-1456.

1075 Romer, R. L., Rötzler, J., 2011. The role of element distribution for the isotopic
1076 dating of metamorphic minerals. *European Journal of Mineralogy*, 23, 17-33.

1077 Romer, R.L., Schärer, U., Steck, A., 1996. Alpine and pre-Alpine magmatism in the
1078 root-zone of the western Central Alps. *Contributions to Mineralogy and Petrology*, 123,
1079 138-158.

1080 Romer, R.L., Siegesmund, S., 2003. Why allanite may swindle about its true age.
1081 *Contributions to Mineralogy and Petrology*, 146, 297-307.

1082 Rubatto, D., 2002. Zircon trace element geochemistry: partitioning with garnet and
1083 the link between U-Pb ages and metamorphism. *Chemical Geology*, 184, 123-138.

1084 Rubatto, D., 2017. Zircon: the metamorphic mineral. *Reviews in Mineralogy and*
1085 *Geochemistry*, 83, in press.

1086 Rubatto, D., Chakraborty, S., Dasgupta, S., 2013. Timescales of crustal melting in the
1087 Higher Himalayan Crystallines (Sikkim, Eastern Himalaya) inferred from trace element-
1088 constrained monazite and zircon chronology. *Contributions to Mineralogy and*
1089 *Petrology*, 165, 349-372.

1090 Rubatto, D., Hermann, J., Berger, A., Engi, M., 2009. Protracted fluid-induced
1091 melting during Barrovian metamorphism in the Central Alps. *Contributions to*
1092 *Mineralogy and Petrology*, 158, 703-722.

1093 Rubatto, D., Regis, D., Hermann, J., Boston, K., Engi, M., Beltrando, M., McAlpine,
1094 S.R.B., 2011. Yo-yo subduction recorded by accessory minerals in the Italian Western
1095 Alps. *Nature Geoscience*, 4, 338-342.

1096 Rützi, R., Marquer, D., Thompson, A.B., 2008. Tertiary tectono-metamorphic
1097 evolution of the European margin during Alpine collision: example of the Leventina
1098 Nappe (Central Alps, Switzerland). *Swiss Journal of Geoscience*, 101, S157-S171.

1099 Schlunegger, F., 1999. Controls of surface erosion on the evolution of the Alps:

1100 constraints from the stratigraphies of the adjacent foreland basins. *International Journal*
1101 *of Earth Sciences*, 88, 285-304

1102 Schmid, S., Aebli, H.R., Heller, F., Zingg, A., 1989. The role of the Periadriatic Line in
1103 the tectonic evolution of the Alps. In M.P. Coward, D. Dietrich, R.G. Park (Eds.),
1104 *Conference on Alpine tectonics. Geological Society Special Publications*, 45, 153-171.

1105 Shaw, D.M., 1956. Geochemistry of pelitic rocks. Part III: major elements and
1106 general geochemistry. *Geological Society of America Bulletin*, 67, 919-934.

1107 Smith, H.A., Barreiro, B., 1990. Monazite U-Pb dating of staurolite grade
1108 metamorphism in pelitic schists. *Contributions to Mineralogy and Petrology*, 105, 602-
1109 615.

1110 Smye, A.J., Roberts, N.M.W., Condon, D.J., Horstwood, M.S.A., Parrish, R.R., 2014.
1111 Characterising the U-Th-Pb systematics of allanite by ID and LA-ICPMS: Implications for
1112 geochronology. *Geochimica et Cosmochimica Acta*, 135, 1-28.

1113 Spear, F.S., 2010. Monazite–allanite phase relations in metapelites. *Chemical*
1114 *Geology*, 279, 55-62.

1115 Spear, F.S., Pyle, J.M., 2010. Theoretical modelling of monazite growth in a low-Ca
1116 metapelite. *Chemical Geology*, 273, 111-119.

1117 Stacey, J.S., Kramers, J.D., 1975. Approximation of terrestrial lead isotope evolution
1118 by a two-stage model. *Earth and Planetary Science Letters*, 26, 207-221.

1119 Steck, A., Della Torre, F., Keller, H., Pfeifer, H.-R., Hunziker, J., Masson, H., 2013.
1120 Tectonics of the Lepontine Alps: Ductile thrusting and folding in the deepest tectonic
1121 levels of the Central Alps. *Swiss Journal of Geosciences*, 106, 427-450.

1122 Steck, A., Hunziker, J., 1994. The Tertiary structural and thermal evolution of the
1123 Central Alps – compressional and extensional structures in an orogenic belt.
1124 *Tectonophysics*, 238, 229-254.

1125 Todd, C.S., Engi, M., 1997. Metamorphic field gradients in the Central Alps. *Journal*
1126 *of metamorphic Geology*, 15, 513-530.

1127 Trommsdorff, V., 1980. V. General questions. 1. Alpine metamorphism and Alpine
1128 intrusions. In R. Trümpy (Ed.), *Geology of Switzerland: a guide book. Part A: An outline*
1129 *of the Geology of Switzerland* (pp. 82-87). Basel: Wepf & Co.

1130 Trommsdorff, V., Hermann, J., Müntener, O., Pfiffner, M., Risold, A.-C., 2000.
1131 Geodynamic cycles of subcontinental lithosphere in the Central Alps and the Arami
1132 enigma. *Journal of Geodynamics*, 30, 77-92.

1133 Vance, D., O'Nions, R.K, 1992. Prograde and retrograde thermal histories from the
1134 central Swiss Alps. *Earth and Planetary Science Letters*, 114, 113-129.

1135 von Blanckenburg, F., 1992. Combined high-precision chronometry and
1136 geochemical tracing using accessory minerals: applied to the Central-Alpine Bergell
1137 intrusion (central Europe). *Chemical Geology*, 100, 19-40.

1138 Vonlanthen, P., Fitz Gerald, J.D., Rubatto, D., Hermann, J., 2012. Recrystallization
1139 rims in zircon (Valle d'Arbedo, Switzerland): An integrated cathodoluminescence, LA-
1140 ICP-MS, SHRIMP, and TEM study. *American Mineralogist*, 97, 369-377.

1141 Vry, J.K. Baker, J.A., 2006. LA-MC-ICPMS Pb–Pb dating of rutile from slowly cooled
1142 granulites: Confirmation of the high closure temperature for Pb diffusion in rutile.
1143 *Geochimica et Cosmochimica Acta* 70, 1807-1820.

1144 Wang, J.-M., Rubatto, D., Zhang, J.-J., 2015. Timing of partial melting and cooling
1145 across the Greater Himalayan Crystalline Complex (Nyalam, central Himalaya): in-
1146 sequence thrusting and its implications. *Journal of Petrology*, 56, 1677-1702.

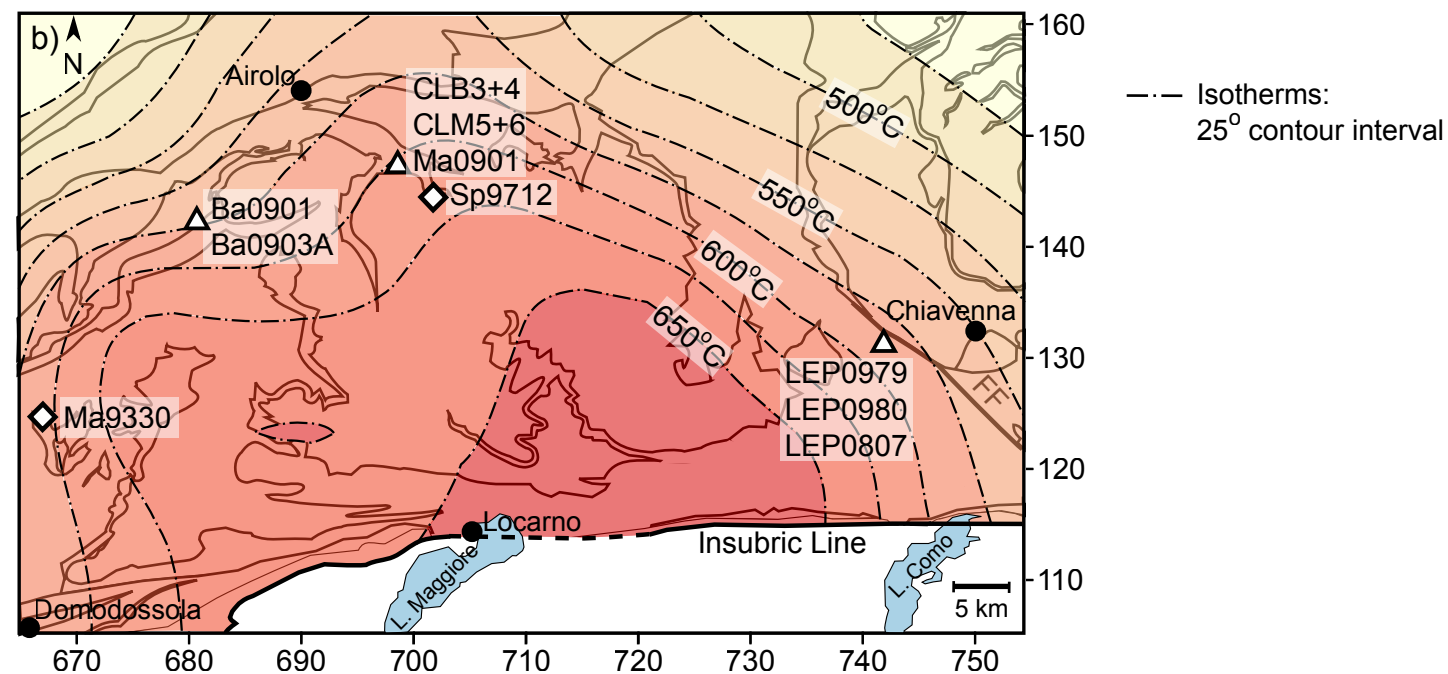
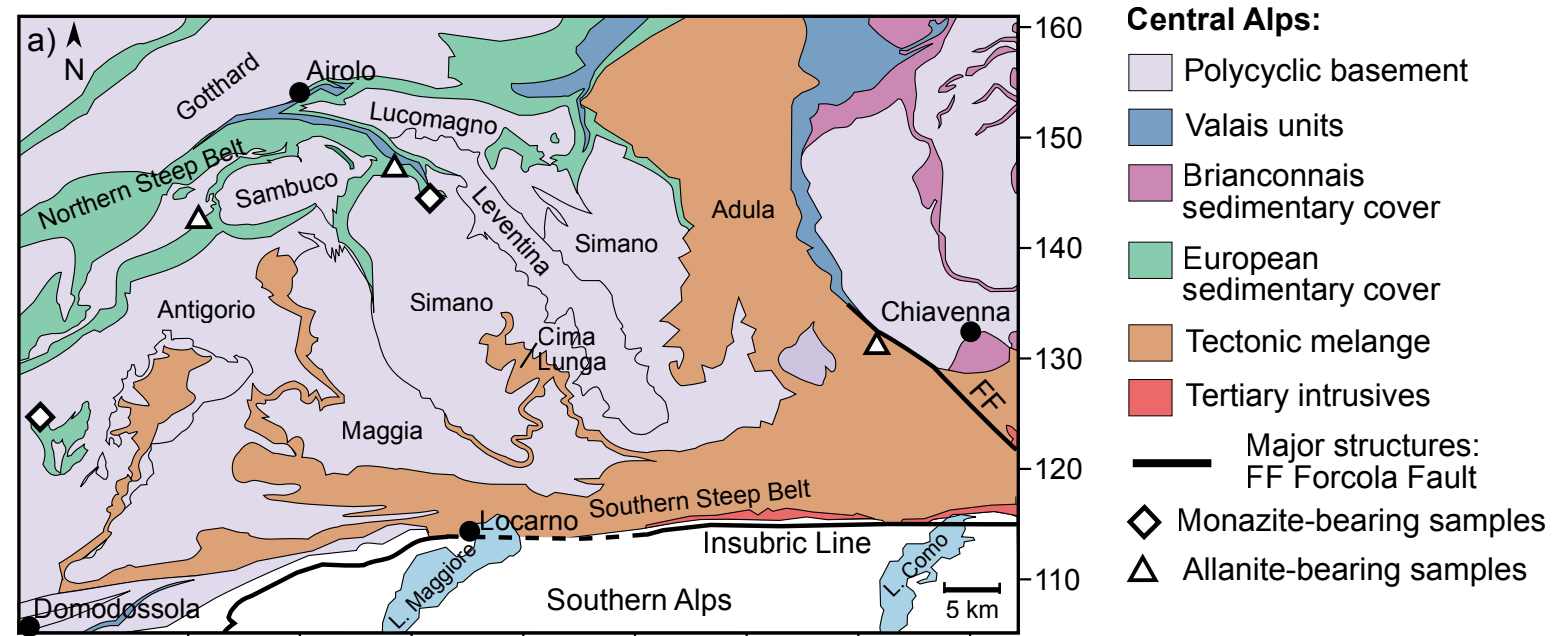
1147 Warren, C. J., Grujic, D., Cottle, J. M., Rogers, N. W., 2012. Constraining cooling
1148 histories: rutile and titanite chronology and diffusion modelling in NW Bhutan. *Journal*
1149 *of Metamorphic Geology*, 30, 113-130.

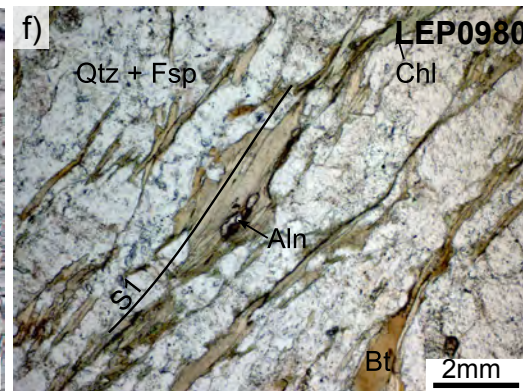
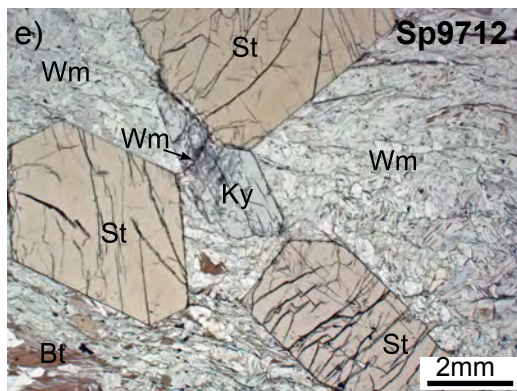
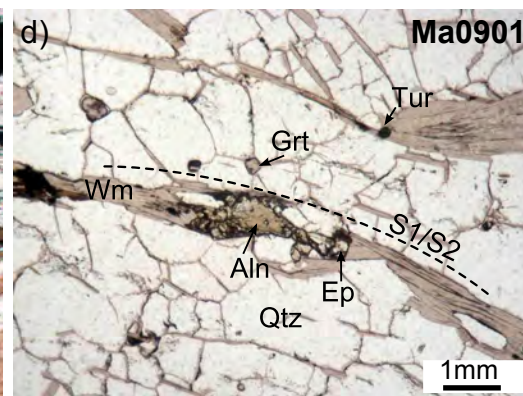
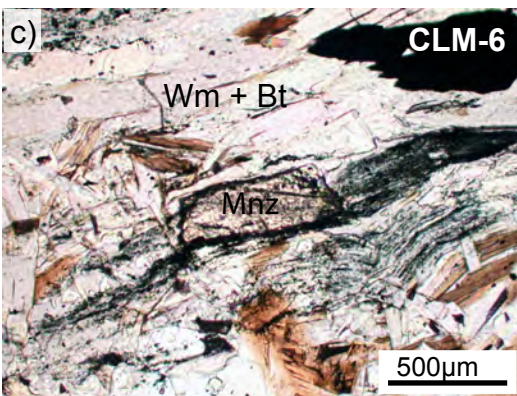
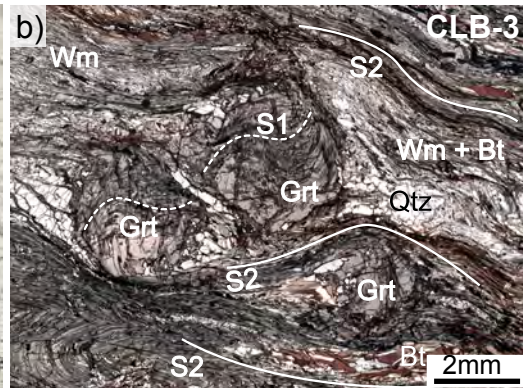
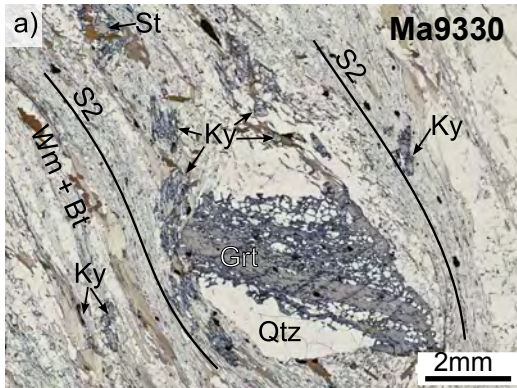
1150 Wiederkehr, M., Bousquet, R., Schmid, S.M., Berger, A., 2008. From subduction to
1151 collision: thermal overprint of HP/LT meta-sediments in the north-eastern Lepontine
1152 Dome (Swiss Alps) and consequences regarding the tectono-metamorphic evolution of
1153 the Alpine orogenic wedge. *Swiss Journal of Geoscience*, 101, S127-155.

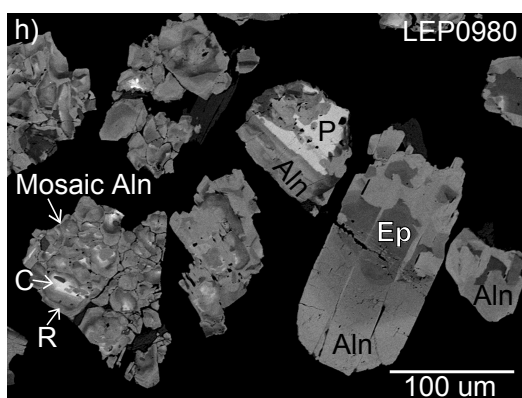
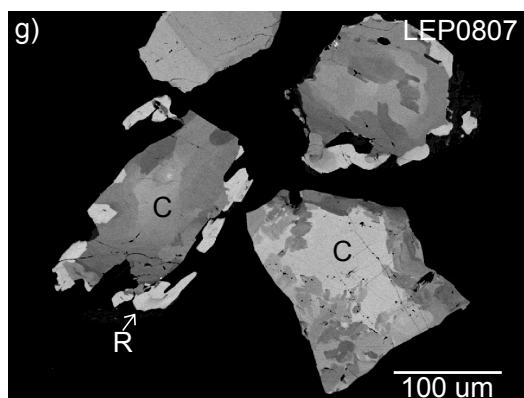
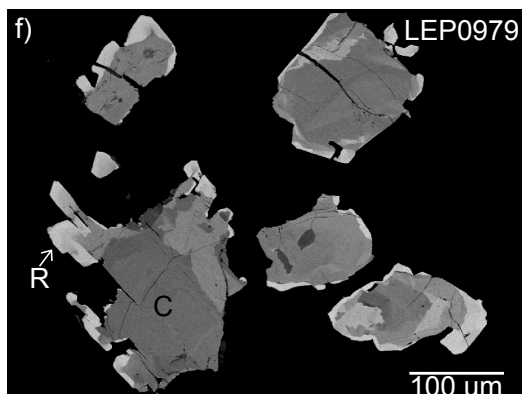
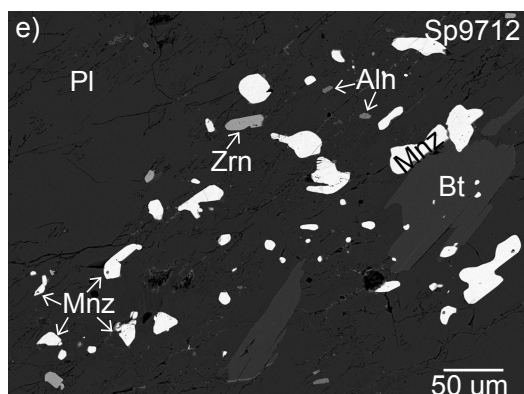
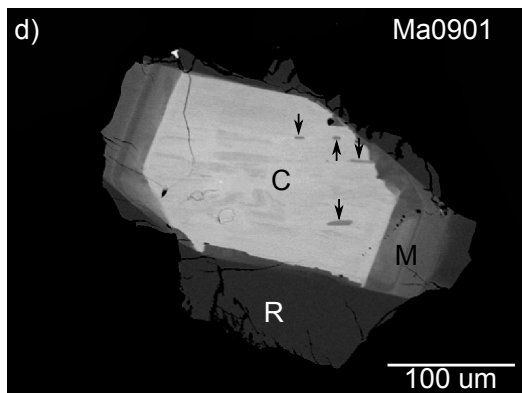
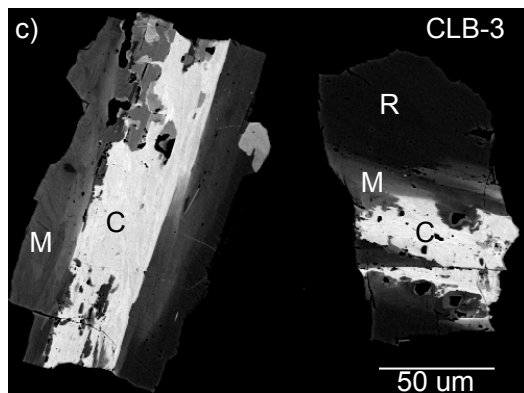
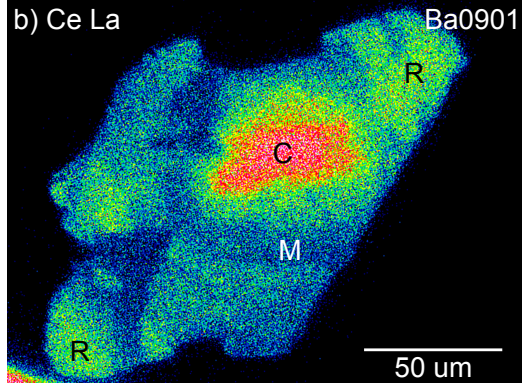
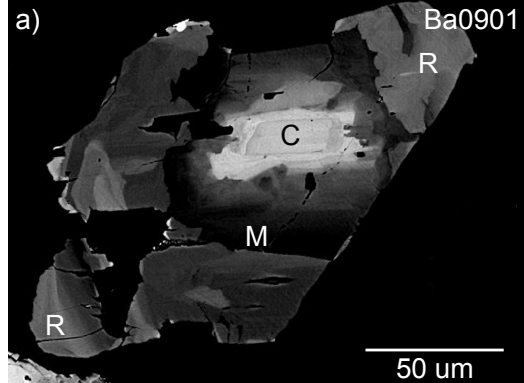
1154 Wiederkehr, M., Sudo, M., Bousquet, R., Berger, A., Schmid, S.M., 2009. Alpine
1155 orogenic evolution from subduction to collisional thermal overprint: The $^{40}\text{Ar}/^{39}\text{Ar}$ age
1156 constraints from the Valaisan Ocean, central Alps. *Tectonics*, 28, TC6009.

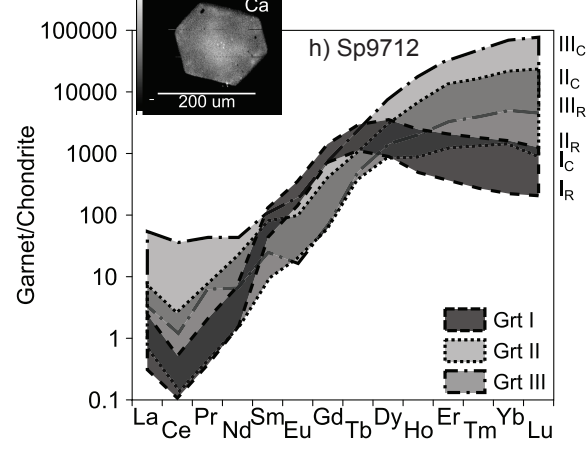
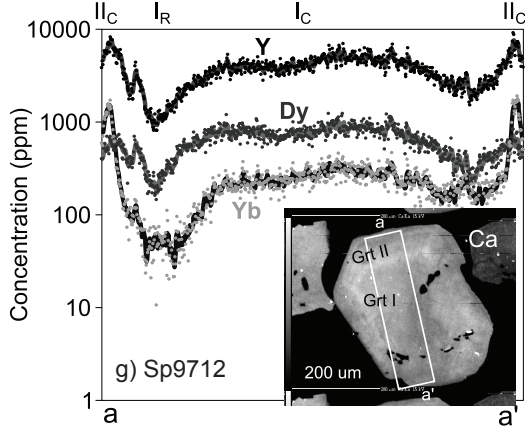
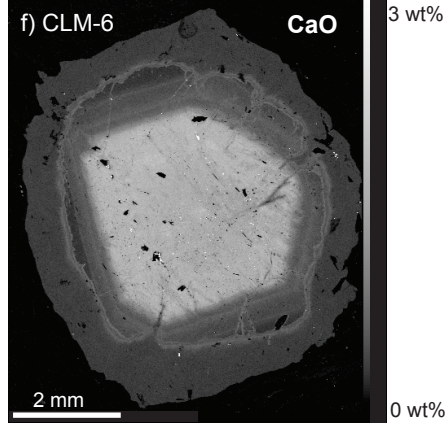
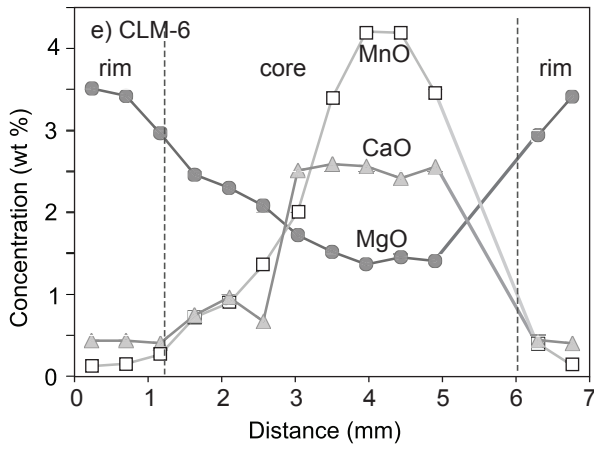
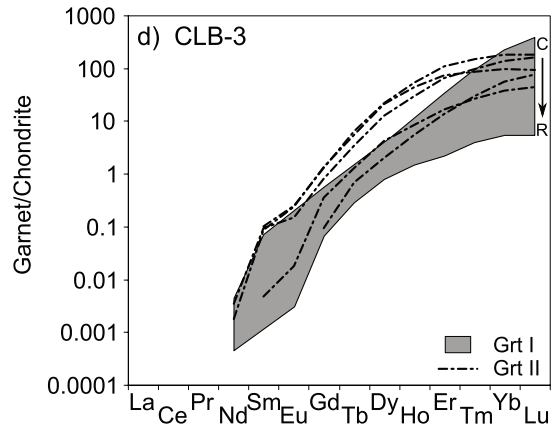
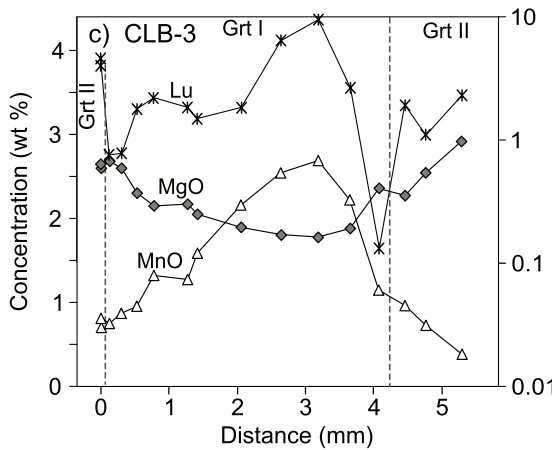
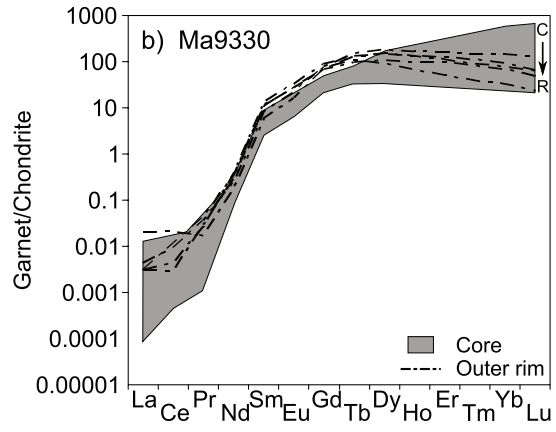
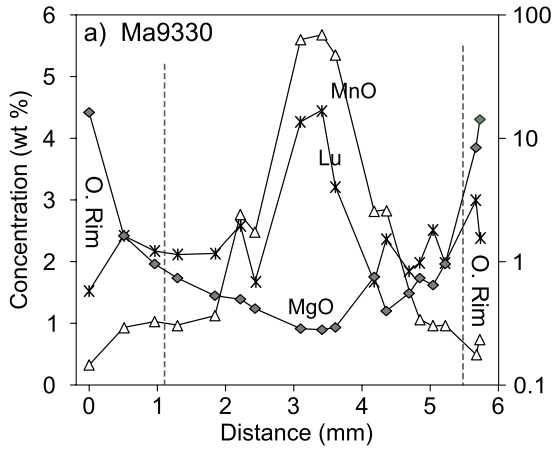
1157 Wiederkehr, M., Bousquet, R., Ziemann, M. A., Berger, A., Schmid, S., 2011. 3-D
1158 assessment of peak-metamorphic conditions by Raman spectroscopy of carbonaceous
1159 material: an example from the margin of the Lepontine dome (Swiss Central Alps).
1160 *International Journal of Earth Sciences*, 100, 1029-1063.

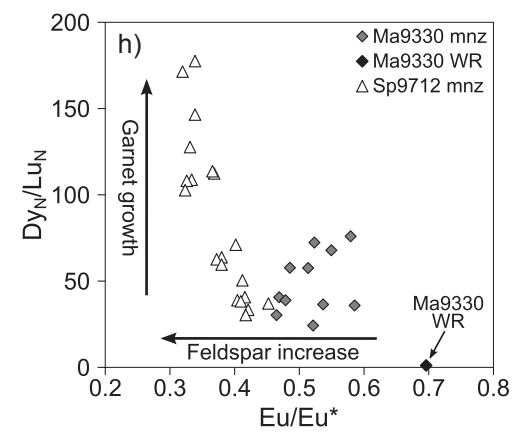
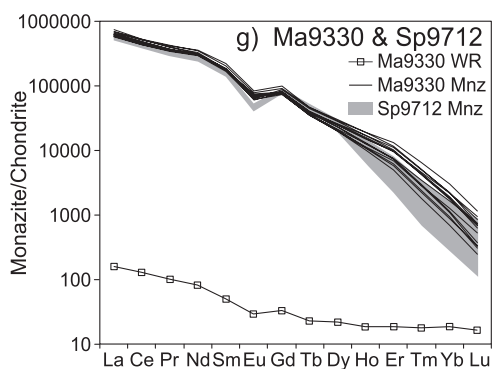
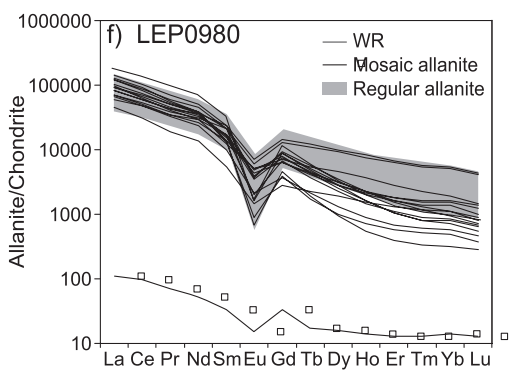
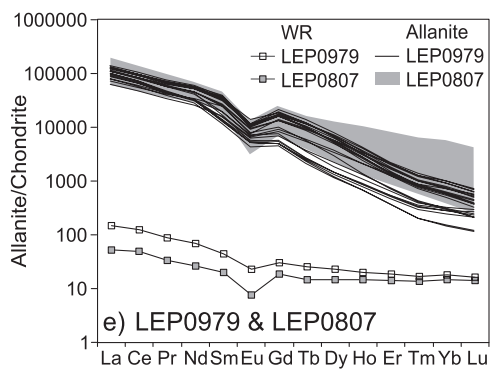
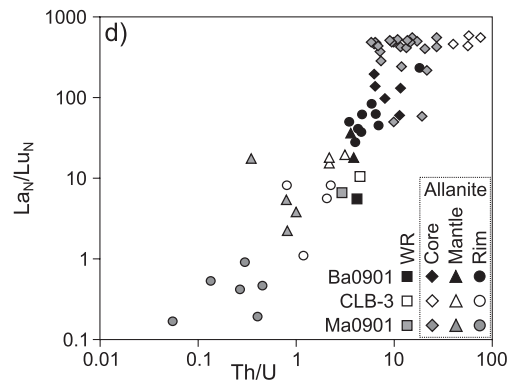
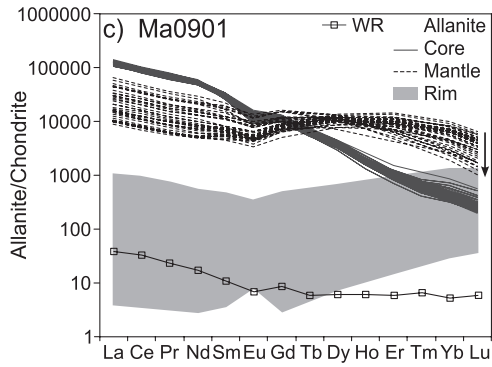
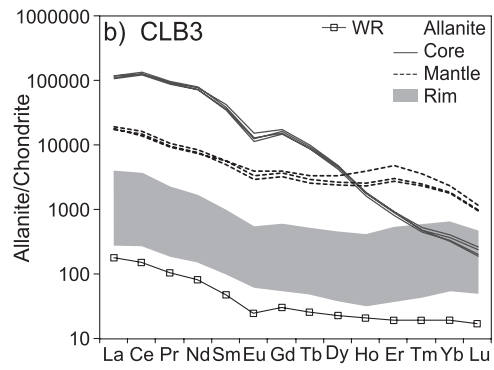
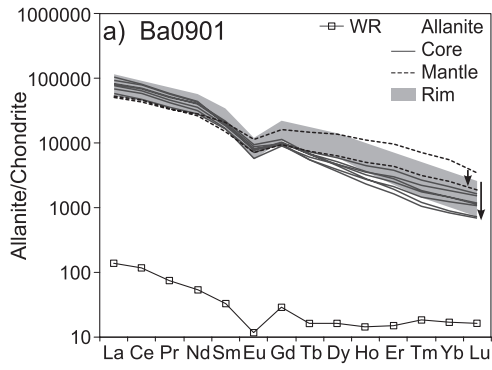
1161 Wing, B.A., Ferry, J.M., Harrison, T.M., 2003. Prograde destruction and formation of
1162 monazite and allanite during contact and regional metamorphism of pelites: petrology
1163 and geochronology. *Contributions to Mineralogy and Petrology* 145, 228-250.

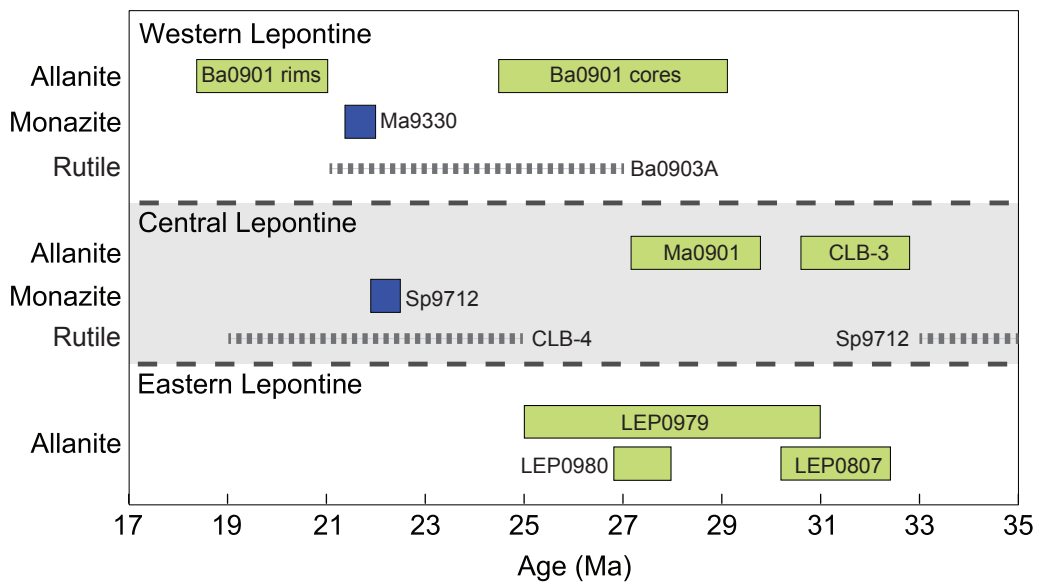


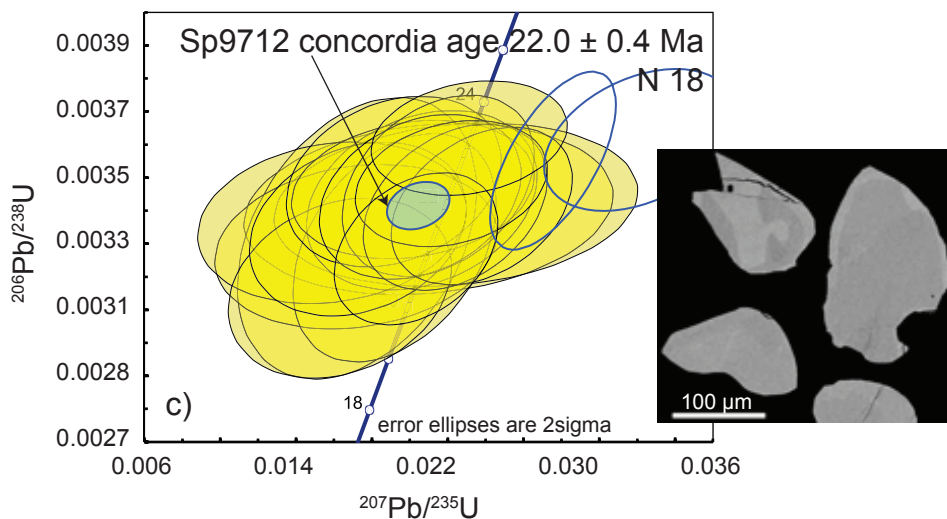
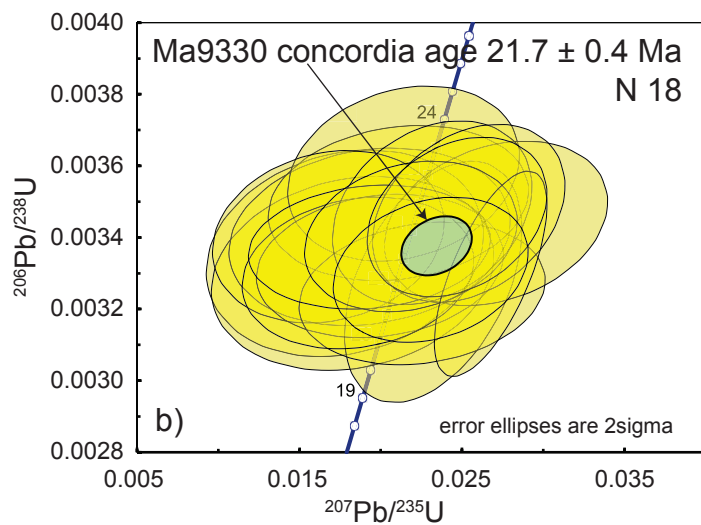
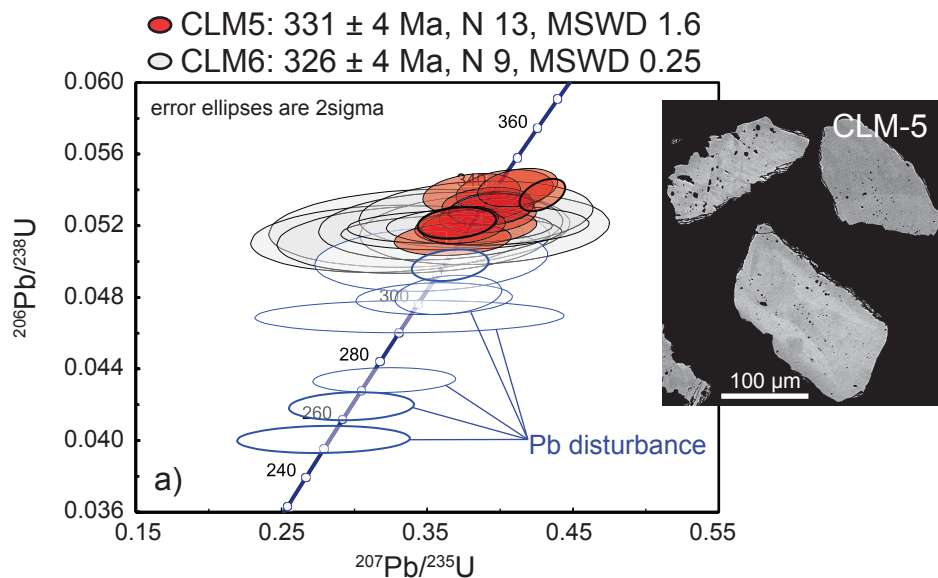


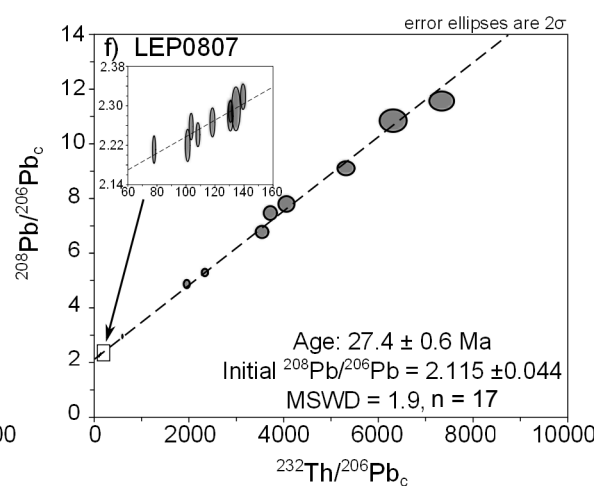
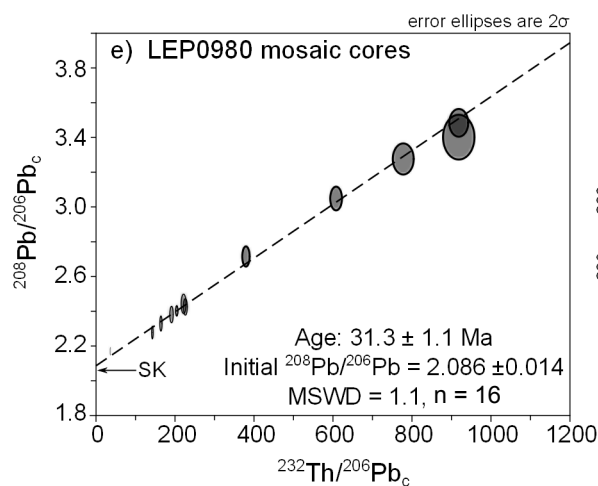
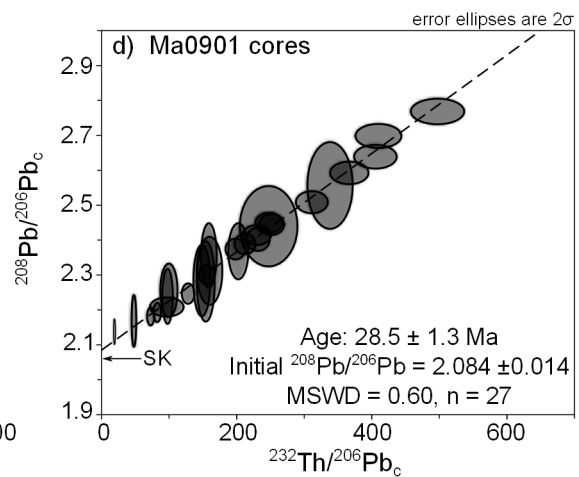
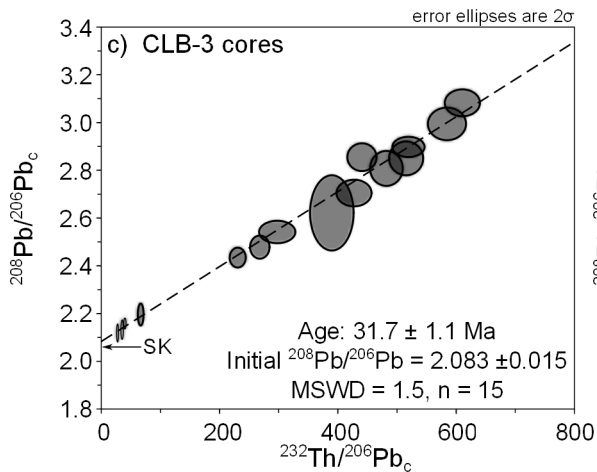
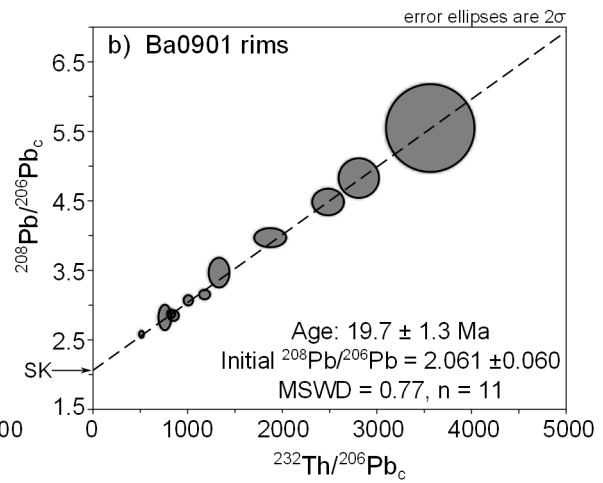
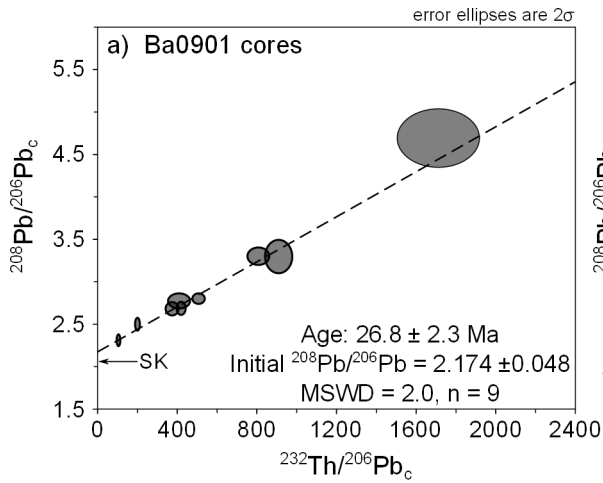


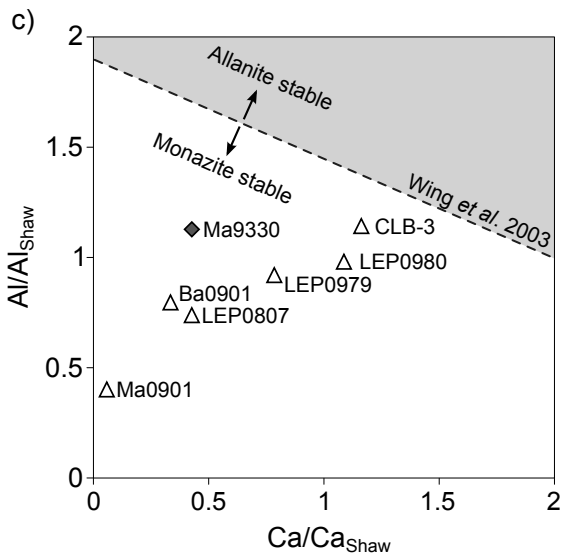
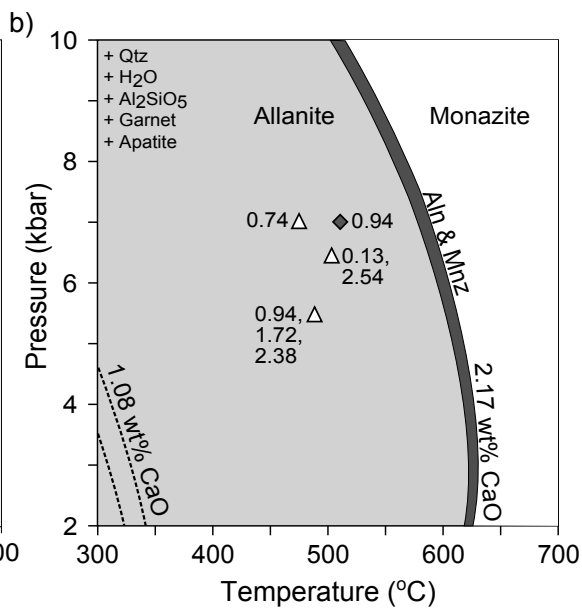
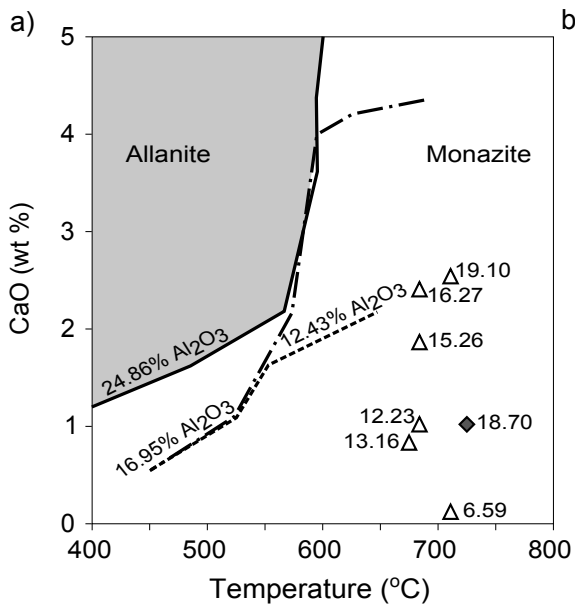




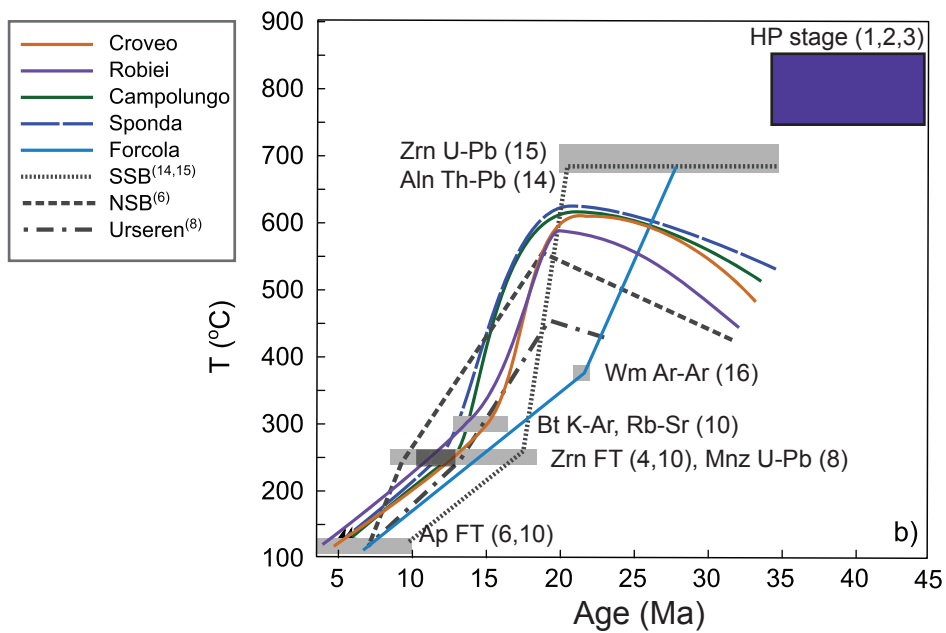
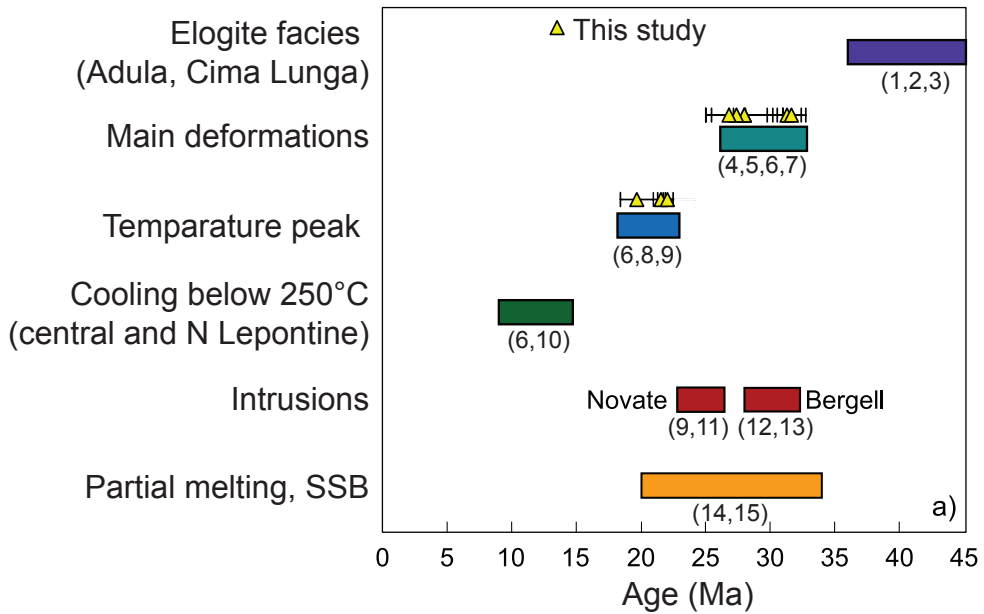








- △ Allanite-bearing sample
- ◆ Monazite-bearing sample



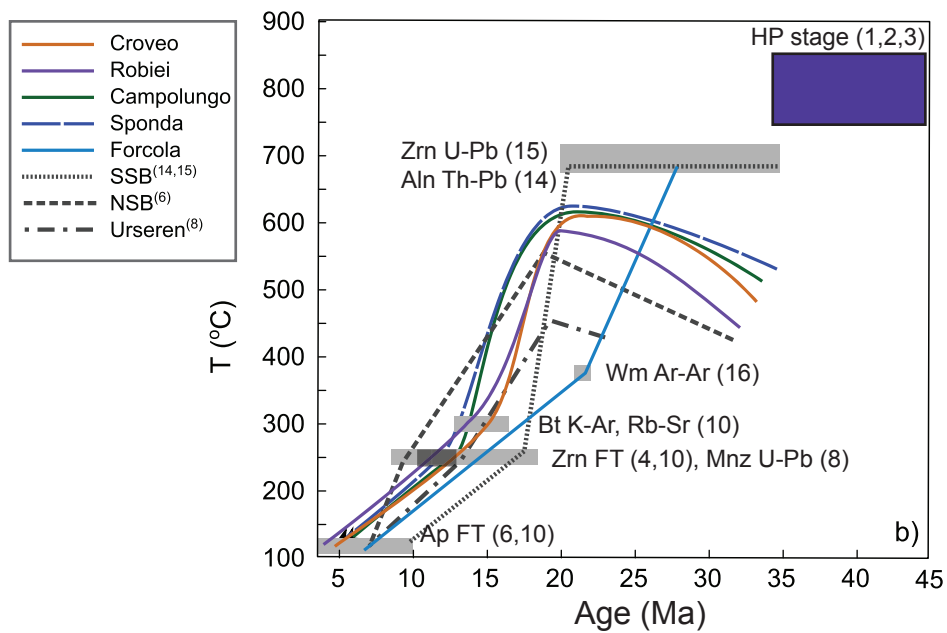
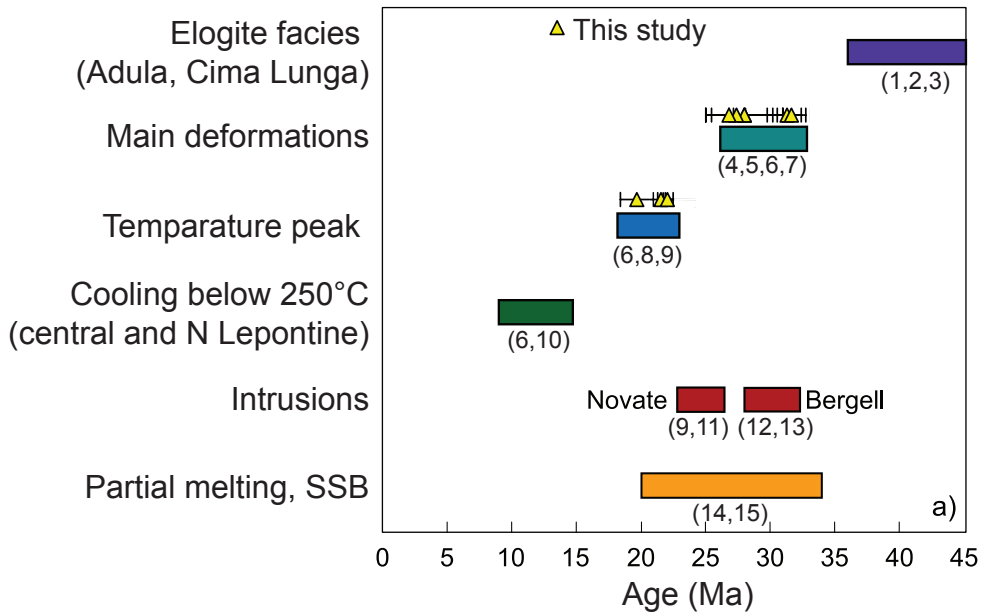


Table 1: Sample overview showing the main and accessory mineral assemblage, the minerals used for dating and the results of U-Th-Pb geochronology.

Sample	Swiss Grid coordinates		Location	Rock type	Mineral assemblage			Mineral dated	Age (Ma)
	X	Y			Main	Accessory			
Ma9330 ¹	666.51	124.88	Croveo, (N of Domodossola)	Metapelite	Qtz Wm Bt Pl Grt St Ky	Mnz Ap Rt Ilm Zrn	Mnz	21.7 ± 0.4	
Ba0903A	682.20	143.37	Robiei	Metapelite "Bündnerschiefer"	Qtz, Wm Bt Pl Grt Cal	Aln Rt Ilm Zrn	Rt	(21–27) ³	
Ba0901	683.23	142.70	Robiei	Gneiss	Qtz Wm Bt Kfs Pl	Aln Ap Zrn Rt	Aln cores	26.8 ± 1.3	
							Aln rims	19.7 ± 1.3	
CLB-3	697.37	147.60	Campolungo	Metapelite "Bündnerschiefer"	Qtz Wm Bt Pl Grt	Aln Rt Zrn	Aln	31.7 ± 1.1	
CLB-4	697.37	147.60	Campolungo	Metapelite "Bündnerschiefer"	Qtz Wm Bt Pl Grt Ky St	Aln Rt Zrn	Rt	(19–25) ³	
CLM-5	698.04	146.94	Campolungo	Metasediment, basement	Qtz Wm Bt Pl Grt St Ky	Zrn Mnz Tur	Mnz	332 ± 4	
CLM-6	698.82	146.66	Campolungo	Metasediment, basement	Qtz Wm Bt Pl Grt St	Zrn Mnz	Mnz	326 ± 4	
Ma0901	698.29	147.23	Campolungo	Metaquartzite	Qtz Wm Bt Pl Grt	Ap Aln Rt Zrn	Aln	28.5 ± 1.3	
Sp9712	702.78	142.20	Alpe Sponda	Metasediment, basement	Qtz Wm Bt Pl Grt St Ky	Mnz Rt Zrn	Mnz	22.0 ± 0.4	
							Rt	(57–33) ³	
LEP0979 ²	743.95	130.70	Forcola	Orthogneiss	Qtz Wm Bt Kfs Pl	Aln Zrn	Aln	25–31	
LEP0980 ²	744.05	131.24	Forcola	Orthogneiss	Qtz Wm Bt Chl Kfs Pl	Aln Zrn	Mosaic Aln	31.3 ± 1.1	
							Regular Aln	27–31	
LEP0807 ²	744.18	131.38	Forcola	Orthogneiss	Qtz Wm Bt Chl Kfs Pl	Aln Zrn	Aln	27.4 ± 0.6	

¹ Ma9330 is the sample used in Todd & Engi, 1997

² LEP0807, -0979 and -0980 were donated by C Augenstein

³ These are not formation ages, but dates that may include inheritance and Pb loss after formation, see text for discussion.

Appendix

1. Sample description

Western Samples: Croveo (Ma9330) and Robiei (Ba0901, BA0903A)

Sample Ma9330 is the highest-grade rock of the western samples and reached T_{\max} of ~ 620 °C (617 ± 11 °C for this sample in Todd and Engi, 1997). The rock is characterised by inclusion-rich garnet porphyroblasts, rotated in the foliation (Fig. 2a), and rounded staurolite and kyanite (see also sample description in Todd and Engi, 1997). Inclusions in garnet are mainly quartz with minor ilmenite and relic allanite. Allanite is not present in the matrix; monazite, which displays no zoning in BSE images, is a matrix mineral and has not been observed as inclusion in garnet. The bulk rock composition is similar to that of the Campolungo calcschist (Bündnerschiefer CLB-3), except that it has a lower CaO concentration and Ca/Al ratio (Table A1).

Three foliations are present in Ma9330. In schist Ma9330 S1 is a relic foliation defined by the alignment of kyanite and staurolite, overprinted by a sub-parallel S2 fabric defined by mica that wraps around kyanite, staurolite and garnet (Fig. 2a). A texturally later weak foliation (S3) is defined by sparse biotite that tends to be smaller than S2 biotite.

Robiei samples Ba0901 and Ba0903A are from an area that reached significantly lower T_{\max} than Ma9330 during Barrovian metamorphism ($T_{\max} \sim 575$ °C according to the regional T distribution of Todd and Engi, 1997). Calcschist Ba0903A contains white mica, biotite, plagioclase and large poikiloblastic garnets (similar to those found in Ma9330), but lacks both staurolite and kyanite. Minor calcite occurs in low-strain bands comprised

predominantly of quartz. Ba0901 is a fine-grained gneiss containing mm-sized porphyroblasts of K-feldspar and quartz, wrapped in a matrix of feldspars, quartz, biotite and muscovite. The bulk composition of Ba0901 gneiss closely resembles the orthogneiss samples in terms of Al and Na and is low in Ca and Ca/Al (CaO = 0.7 wt%, Ca/Al = 0.08; Table A1). Ba0901 allanite is characterised by cores with high BSE emission that are surrounded by mantle zones, which are overgrown by allanite rims (Fig. 3a-b). The mantle domains change from allanitic compositions near the core, to more epidote compositions towards the rim. The allanite core and epidote mantle are partially replaced by a second generation of allanite at the rim; allanite rims form a sharp contact with the mantle. Both core and rim allanite have inclusions of muscovite and biotite.

In Ba0903A, S1 is a relic foliation that is overprinted by sub-parallel S2. S1 is defined by the alignment of mica and allanite-epidote that is preserved in garnet; S2 is distinguished from the relic foliation as it wraps around garnet. S3 a weak foliation that is defined by a few biotite grains and crosscuts S1 and S2 at a high angle. Ba0901 displays only one strong foliation (likely to be S1/S2), which is defined by the alignment of muscovite and biotite, and that also contains allanite. The foliation is overgrown by a second generation of larger grains of biotite and white mica that have no preferred orientation.

Central samples: Campolungo (CLB-3, CLB-4, Ma0901, CLM-5 and CLM-6) and Alpe Sponda (Sp9712)

Calcschists CLB-3 and CLB-4, and impure quartzite Ma0901 are from the Campolungo area, southeast of Airolo (Fig. 1). CLB-3 represents a pelitic layer within the Bündnerschiefer. It has the highest CaO concentration of the samples

analysed for bulk composition ($\text{CaO} = 2.5 \text{ wt } \%$) and a high Ca/Al ratio of 0.18 (Table A1). Typical of Bündnerschiefer, CLB-3 hosts mm-to-cm sized garnet porphyroblasts in a fine-grained grey-blue matrix that is predominantly biotite, white mica, plagioclase and quartz (Fig. 2b). Accessory allanite occurs as cores in large ($> 200 \mu\text{m}$) epidote grains that have three distinct zones: small cores ($< 100 \mu\text{m}$) with high BSE emission, a mantle zone ($< 50 \mu\text{m}$ or absent) of lower emission, and an epidote rim (Fig. 3c). In sample CLB-3, S1 is a relic foliation defined by the alignment of mica and allanite preserved in garnet (Fig. 2b). S2 is the dominant foliation and it is defined by biotite and white mica that wrap garnet and allanite-epidote grains. S2 is folded and axial-planar biotite and white mica form a third foliation (S3). CLB-4 contains staurolite and kyanite in addition to garnet, white mica, biotite, plagioclase, and accessory allanite, rutile and zircon. Textural relationships and foliations are similar to CLB-3. In CLB-4, staurolite and plagioclase both overgrow folded white mica and biotite.

Ma0901 is a mica-rich impure quartzite ($\text{SiO}_2 = 88 \%$) with low CaO content ($0.13 \text{ wt. } \%$) and $\text{Ca}/\text{Al} = 0.03$ (Table A1). This sample was collected between the prominent dolomite marble bands representing the Triassic sediments and the Simano basement (Fig. 1a). The protholith of Ma0901 is most likely a Permian sandstone. Bands of muscovite host tourmaline, rutile and allanite-epidote (Fig. 2d). Garnets are small, rare and occur exclusively in low-strain bands of quartz; no relic foliation is preserved in the small garnets. Similar to CLB-3 calcschist allanites, Ma0901 allanite grains display three distinct growth zones (Fig. 3d). Large cores (up to $\sim 300 \mu\text{m}$) are host to rutile, muscovite and biotite inclusions. Mantle zones have intermediate BSE emission and often show oscillatory zoning; epidote rims have low BSE emission. There is

one foliation preserved in Ma0901, which is defined by the alignment of muscovite and allanite (Fig. 2d). This foliation is likely to be S1/S2 composite (as S1 and S2 are sub-parallel in the other samples) and it is overgrown by late-stage biotite, chlorite and plagioclase, none of which tend to have a preferred orientation.

CLM-5 and 6 are two staurolite-garnet schists collected a few hundred meters from each other within the Simano nappe. CLM-5 is close to the locality "Fontane" located within the Prevat synform. CLM-6 comes from the Southern end of Laghetto di Campolungo. The metasedimentary rocks in this area have been attributed to late Paleozoic sediments (Permo-Carboniferous) that display chemical characteristics compatible with an active continental margin setting (Gieré et al. 2011). The two samples have a typical amphibolite-facies assemblage. At the cm-dm scale, the samples contain numerous deformed quartz layers alternated by darker layers with a fine-grained crenulated foliation that is defined by muscovite, biotite, quartz, minor plagioclase, ilmenite and graphite. Porphyroblastic garnet is partly wrapped by the main foliation (likely S2), which is folded. Staurolite and kyanite (CLM-5) crystals overgrow the foliation preserving remnants of foliation defined by graphite. CLM-5 also contains abundant tourmaline. Monazite grains are aligned along the main foliation and also contain inclusions of graphite (Fig. 2c).

Sample Sp9712 is from the Alpe Sponda area, a key locality for Alpine kyanite. The sample is from the base of Monte Forno, situated within the Campo Tencia polymetamorphic basement that is considered part of the Simano nappe (Steck et al. 2013). The locality also exposes ortho-amphibolites and calc-silicate

nodules, which are typical of basement units in the gneiss nappes. Sp9712 is a coarse-grained granofels that has two compositional layers: one predominantly kyanite and staurolite, with muscovite, paragonite, and minor biotite and plagioclase; the other is almost exclusively biotite and plagioclase. The staurolite-kyanite layer is characterised by millimetre-to-centimetre scale staurolite and kyanite. Two generations of kyanite are apparent and the older kyanite grains are partly replaced by white mica (Fig. 2e); the second kyanite generation displays sharp grain edges and shows no signs of replacement. Sp9712 garnet is relatively small ($< 500 \mu\text{m}$), sparse, and occurs only in plagioclase within the biotite-rich compositional layer. Garnet contains inclusions of relic allanite but not monazite. Unlike the samples from Campolungo, Sp9712 has no dominant foliation in thin section or hand-specimen scale: large staurolite and kyanite are randomly orientated, as are the white mica and biotite grains in both compositional domains.

Accessory rutile and monazite occur in both compositional layers in Sp9712. Rutile occurs in the matrix and as inclusions in staurolite and garnet. Monazite often occurs in groups of more than five grains, sometimes as satellites surrounding a small ($\sim 10 \mu\text{m}$) relic allanite grain (Fig. 3e). Monazite can also contain inclusions of relic allanite. Monazite grains are subtly heterogeneous in BSE images and display either patchy or core-rim zoning.

Eastern samples: Forcola orthogneiss (LEP0979, LEP0980, LEP0807)

The eastern-most samples are orthogneisses from the Adula nappe in the footwall of the Forcola fault (Fig. 1). Samples LEP0979 and LEP0807 are predominantly quartz, K-feldspar, and white mica with minor plagioclase and

biotite, chlorite, and accessory allanite and zircon. LEP0980 differs only in that biotite predominates and white mica is a minor component. In the three samples the major foliation (S1) is defined by the alignment of white mica (LEP0979 and LEP0807) or biotite (LEP0980, Fig. 2f), which are overgrown by larger micas belonging to a later metamorphic stage. In all three samples, allanite is aligned along the major foliation (S1). Neither garnet nor rutile is present in any of the orthogneiss samples. Forcola orthogneiss has CaO concentrations that vary from 0.9–2.4 wt % (Table A1). Ca/Al ratios are at the higher end of the analysed values (0.1–0.2).

LEP0979 and LEP0807 allanite occurs as overgrowths with high BSE emission on patchy or oscillatory-zoned epidote grains (Fig. 3f). LEP0807 allanite can also form large cores in patchy grains (Fig. 3g). Sample LEP0980 contains allanite with a variety of textures (Fig. 3h). Pre-Alpine igneous allanites (~250 Ma, see below) are weakly zoned in BSE images and can have small, presumably metamorphic overgrowths. Alpine allanites have vastly different internal zoning and are divided into two groups: mosaic and regularly zoned allanites. Regularly zoned allanite can occur as single grains, locally with weak oscillatory zoning or as overgrowths on epidote grains. Unique “mosaic” grains are aggregates of several small allanite sub-grains. Mosaic allanites are further subdivided into early (mosaic core) and late (mosaic rim) domains, according to the internal zoning and overprinting relationships within the subgrains (C and R in Figure 3h).

2. Methods

Bulk rock analysis

Bulk rock analysis was conducted at the Central Analytical Facilities, Stellenbosch University, South Africa. Samples were milled in an agate mill before being mixed with CLAISSE flux (1 g sample to 10 g flux) and fused into a lithium borate disc. Si, Ti, Al, Fe, Ca, Mg, Mn, Na, K and P were measured by XRF of fused discs using an Axios (PANalytical) with a 2.4 kWatt Rh tube. Trace elements were analysed by LA ICPMS (method outlined below).

Scanning Electron Microscope (SEM) and electron microprobe

Back scattered electron (BSE) images of minerals in thin section and polished grain mounts were made using the JEOL 6400 SEM (15 kV, WD 39 mm), the Cambridge 360 (20kV, 3nA, WD 15 mm) at the Centre for Advanced Microscopy at the Australian National University (ANU), and the JEOL JSM 6610A (15 kV, WD 10-15 mm) at the Research School of Earth Sciences (RSES), ANU. The EDS-detector on the JEOL 6400 was also used for mineral identification and for quantitative x-ray analysis of major phases.

Electron microprobe spot analyses of allanite and element maps of garnet were made using the Cameca SX 100 at the ANU. Accelerating voltage was 15 kV with a current of 100 nA. Elements analysed were Si (K- α), Ti (K- α), Al (K- α), Fe (K- α), Mn (K- α), Mg (K- α), Ca (K- α), Y (L- α), La (L- α), Ce (L- α), Pr (L- β), Nd (L- β), Sm (L- β), Th (M- α) and U (M- β). The background positions were carefully selected after line-scans on trace element-rich allanites in order to avoid interferences. Daibosatsu allanite (Hoshino et al. 2005) and Fukudayama allanite

(Hoshino et al. 2006) were used as secondary standard to check within-session variability. Values for Daibosatsu allanite were within 1 wt % of published values for all elements analysed, whereas Fukudayama allanite analyses were within 1 wt % for elements measured except for Si, Fe and Th. Si and Th were within 1.5 wt % and Fe was within 3 wt % of published values (Hoshino et al. 2006). The same beam set up conditions were used for making element maps of garnet at ANU. The dwell time on each spot was 100 ms with a step interval of 1 μm .

LA-ICP-MS trace element analysis

Trace element analysis was made on polished epoxy grain mounts, thin sections and bulk rock glasses using an Agilent 7500s and 7700 quadrupole inductively coupled plasma mass spectrometer (ICP-MS) in peak-jumping mode, attached to an ArF excimer laser (193 nm wavelength, at 5 Hz) system at RSES. Samples were loaded into a purpose-built HelEx ablation cell and ablation was carried out in a He atmosphere (Eggins et al. 1998). An analysis consisted of 20-30 seconds of background gas analysis, followed by 30-45 seconds of ablation. Contamination by inclusions, drill through or alteration was determined by monitoring several pertinent elements during the time-resolved analysis and only the relevant part of the analysis was included in the integration.

Analyses of bulk rock glasses were made using a 108 or 178 μm spot. The analysis spot diameter was 22 μm for allanite and monazite, 47 or 81 μm for garnet, 37 or 47 μm for rutile depending on the size of the grains.

Traverses of Sp9712 garnets were made by scanning a slit ~ 10 μm long across the sample at a rate of ~ 1 $\mu\text{m}/\text{second}$ (Spandler et al. 2007). Where possible, the slit was aligned parallel to internal zoning of major elements in the

garnet, as revealed by X-ray maps. Synthetic glass standards NIST 610 and 612 were used, with BCR, a natural glass, as a secondary standard. Reference values of Pearce et al. (1997) were used for NIST 612, and from Spandler et al. (2011) for NIST 610. The standard glass was analysed routinely every 10 unknowns. The secondary standard (BCR) was analysed every ~ 20 unknowns and was within 5 % of reference values for elements Ti, V, Mn, Sr, Nb, Ba, La, Pr, Nd, Sm, Eu, Ta, Th, U; within 10% for elements P, Sc, Cr, Zr, Cs, Ce, Gd, Dy, Ho, Er, Yb, Lu, Hf, Pb; and within 15% for Y, Tb and Tm. SiO₂, as determined by electron microprobe, was used as internal standard for allanite, epidote and garnet; stoichiometric Ce and Ti were internal standards for monazite and rutile, respectively (219700 ppm Ce; 599000 ppm Ti). SiO₂ ascertained from XRF analyses was used as the internal standard for bulk rock glasses. Data reduction used the in-house excel spreadsheets written by C Allen, and Iolite (Paton et al. 2011).

SHRIMP U-Th-Pb analysis

Prior to isotope analysis, allanite and monazite were imaged by BSE using the Cambridge 360 and the JEOL JSM 6610A and conditions described above. Allanite was analysed for U, Th and Pb isotopes using SHRIMP RG at RSES. Polished epoxy mounts of standards and unknown grains were analysed by a primary O⁻ ion beam, focussed to a ~ 20 µm spot. Analysis of allanite is similar to zircon (Williams 1998) albeit with the addition of mass 232 (Th) to the run table and the use of the mass peak at 198.9 amu (¹³⁹La²⁸Si¹⁶O) as the reference peak (Gregory et al. 2007). An analysis consisted of six scans through each of the masses. The standardisation procedure to correct for instrumental mass fractionation followed Gregory et al. (2007) and was based on the Th/ThO

versus $^{208}\text{Pb}/^{232}\text{Th}$ correlation instead of the U/UO versus $^{206}\text{Pb}/^{238}\text{U}$ calibration scheme that is commonly used for zircon and monazite.

Two allanite standards were used in each of the analytical sessions. The primary standard TARA (417 Ma; Gregory et al. 2007) was analysed every three unknowns. Calibration errors in each session were between 1.5 and 1.8 % (1σ). The secondary standard BONA (ID-TIMS Th-Pb age: 30.1 ± 0.3 Ma; von Blanckenburg 1992) was used to gauge accuracy. With the exception of three anomalous analyses on domains that displayed subtle patchy zoning, BONA returned a weighted average age of 29.77 ± 0.44 Ma (95 % conf., MSWD = 1.5, $n = 14/17$).

A significant proportion (up to 90%) of the Pb present in metamorphic allanite may be from initial incorporation, and not from the *in situ* decay of U and Th and thus correction for initial Pb becomes extremely important to obtain meaningful ages. Initial Pb (Pb_c) is used here to mean the Pb component initially incorporated into the crystal, which includes common Pb as well as radiogenic Pb inherited from precursor phases. The Th-isochron method is used as it has been demonstrated to give reliable ages that are largely independent of the Pb_c composition, (Gregory et al. 2007; Janots and Rubatto 2014). The initial estimation of $^{206}\text{Pb}_c$ and construction of isochrons follows the method outlined by Gregory et al. (2007) and Janots and Rubatto (2014). ^{207}Pb -corrected single spot dates are presented only where the data do not form a well-constrained isochron, but their geological significance is considered unreliable. The ^{207}Pb -correction used assumes the model common Pb composition of Stacey and Kramers (1975) for initial Pb composition.

Monazite analysis was carried out on SHRIMP II at RSES. Masses analysed are the same as for zircon (Williams 1998), except that mass 202 (Ce phosphate) was used as the reference peak at the beginning of each scan through the masses. Monazite standard USGS44069 was used (424.9 ± 0.4 Ma; Aleinikoff et al. 2006). Energy filtering was used to effectively eliminate isobaric interference on mass 204 (Rubatto et al. 2001), as well as suppressing matrix effects that have been observed in ion probe analysis of monazite (Fletcher et al. 2010). A UO/U versus $^{206}\text{Pb}/^{238}\text{U}$ calibration, as described by Williams (1998), was used for monazite; the calibration error was between 1–1.5 % (1σ). The fraction of non-radiogenic ^{206}Pb (f_{206}) is typically low for monazite and the main source of non-radiogenic Pb is from surface contamination (CLM-5 and 6 0.4–5 %, Ma9330 1.4–3.2 %, Sp9712 0.5–4.5 %). The ^{207}Pb -correction used a Pb composition of Broken Hill galena, which is the approximate composition of common Pb in the laboratory or the model common Pb composition of Stacey and Kramers (1975) and the choice makes no difference to the age results within uncertainty. U-Pb ages are preferred to Th-Pb age because the high counts on the Th peak can compromise its accurate measurement by electron multiplier during SHRIMP analysis and indeed Th ages are more scattered. Data were reduced using Squid 2 (Ludwig 2009) and Isoplot/Ex (Ludwig 2003). All average and isochron ages are given at 95 % confidence level.

Rutile TIMS U-Pb analysis

Dating rutile by isotope dilution U-Pb method was performed at the SPIDE²R lab, RSES, ANU. Hand-picked rutile fractions were cleaned and digested at 190°C in a 4:1 mixture of 25 M HF and concentrated HNO₃ in 3 mL Teflon vials in Parr

Teflon bombs. A mixed U-Pb double spike (^{202}Pb - ^{205}Pb - ^{233}U - ^{236}U) was used as isotopic tracer for rutile unknowns; a ^{205}Pb - ^{233}U - ^{236}U - ^{229}Th spike was used for digestion and column blanks. For the first batch, chemical separation of Pb from rutile followed the established HBr-based protocol (Amelin et al. 2010), where the sample is loaded into the anion exchange column in 0.3M HBr. In the second batch the protocol was modified to use a mixture of 0.3 M HBr + 0.3 M HF was used for the first pass through the columns, in order to assure that Ti stayed in solution and did not precipitate or form colloidal particles. There is no evidence that the different Pb extraction procedures affected the age results. In both batches, samples were loaded into 0.05 ml micro columns packed with Eichrom AG 1x8 200-400 mesh anion exchange resin; Pb was eluted in 0.5 M HNO_3 . The second pass through the columns followed established HBr-based protocols for Pb separation. Separation of U from the matrix was achieved using UTEVA resin and a mixture of 3 M HNO_2 + 1 % H_2O_2 for bulk washes. U was eluted using 0.02 M HNO_3 + 0.2 M HF. Low-U feldspar from the same sample was used for initial Pb correction (composition in Supplementary Table A8b). The established HBr protocol was used for feldspar Pb separation; separation of U was identical to that used for rutile. For the first batch, both U and Pb fractions were loaded onto outgassed Re filaments with Si gel and phosphoric acid for TIMS analysis. The U fractions of the second batch were diluted in 0.2 ml of 0.5 M HNO_3 for analysis by MC-ICPMS.

Pb isotopes were analysed using the Triton Plus Thermal Ionisation Mass Spectrometer (TIMS) at the ANU in static multi-collector mode. Analysis of U isotopes was performed on the Triton TIMS in static multicollector mode (1st batch) and Neptune Plus MC-ICPMS (2nd batch). Calculation of Pb and U in rutile

fractions was made using the excel-based AnySpike (Schmitz and Schoene 2007); data reduction and error propagation of the feldspar fraction was done using PBDAT (Ludwig 1993). Initial Pb corrections were made using the isotopic composition of low-U feldspar from the same sample (see below). Synthetic age standard ET500 (Condon et al. 2008; Huyskens et al. 2016) returned a $^{206}\text{Pb}/^{238}\text{U}$ age of 499.19 ± 0.45 Ma (within 0.2 % of the nominal 500 Ma value).

References for Supplementary Material

Aleinikoff, J.N., Schenck, W.S., Plank, M.O., Srogi, L., Fanning, C.M., Kamo, S.L., Bosbyshell, H., 2006. Deciphering igneous and metamorphic events in high-grade rocks of the Wilmington Complex, Delaware: Morphology, cathodoluminescence and backscattered electron zoning, and SHRIMP U-Pb geochronology of zircon and monazite. *Geological Society of America Bulletin*, 118, 39-64.

Amelin, Y., Kaltenbach, A., Iizuka, T., Stirling, C. H., Ireland, T. R., Petaev, M., Jacobsen, S. B., 2010. U-Pb chronology of the Solar System's oldest solids with variable $^{238}\text{U}/^{235}\text{U}$. *Earth and Planetary Science Letters*, 300, 343-350.

Condon, D, Mclean, N., Schoene, B., Bowring, S., Parrish, R., Noble, S., 2008. Synthetic U-Pb 'standard' solutions for ID-TIMS geochronology. *Geochimica et Cosmochimica Acta*, 72 (12S), A175

Eggins, S.M., Rudnick, R.L., McDonough, W.F. (1998). The composition of peridotites and their minerals: a laser-ablation ICP-MS study. *Earth and Planetary Science Letters*, 154, 53-71.

Fletcher, I.R., McNaughton, N.J., Davis, W.J., Rasmussen, B., 2010. Matrix effects and calibration limitations in ion probe U-Pb and Th-Pb dating of monazite. *Chemical Geology*, 270, 31-44.

Gieré, R., Rumble, D., Günther, D., Connolly, J., Caddick, M.J., 2011. Correlation of growth and breakdown of major and accessory minerals in metapelites from Campolungo, Central Alps. *Journal of Petrology*, 52, 2293-2334.

Gregory, C.J., Rubatto, D., Allen, C.M., Williams, I.S., Hermann, J., Ireland, T., 2007. Allanite micro-geochronology: A LA-ICP-MS and SHRIMP U-Th-Pb study. *Chemical Geology*, 245, 162-182.

Hoshino, M., Kimata, M., Nishida, N., Kyono, A., Shimizu, M., Takizawa, S., 2005. The chemistry of allanite from the Daibosatsu Pass, Yamanashi, Japan. *Mineralogical Magazine*, 69, 403-423.

Hoshino, M., Kimata, M., Shimizu, M., 2006. Allanite-(Ce) in granitic rocks from Japan: genetic implications of patterns of REE and Mn enrichment. *The Canadian Mineralogist*, 44, 45-62.

Huyskens, M.H., Zink, S., Amelin, Y., 2016. Evaluation of temperature-time conditions for the chemical abrasion treatment of single zircons for U-Pb geochronology. *Chemical Geology* 438, 25-35.

Janots, E., Rubatto, D., 2014. U–Th–Pb dating of collision in the external Alpine domains (Urseren zone, Switzerland) using low temperature allanite and monazite. *Lithos*, 184-187, 155-166.

Ludwig, K., 1993. PBDAT: A computer program for processing Pb-U-Th Isotope Data Version 1.24. United States Geological Survey Open File Report, 88-542, 33 p.

Ludwig, K., 2003. Isoplot/Ex version 3.0. A geochronological toolkit for Microsoft Excel (70 pp.) Berkeley: Berkeley Geochronological Centre Special Publication.

Ludwig, K., 2009. SQUID 2: a user's manual, rev. 12 Apr, 2009 (110 pp.). Berkeley: Berkeley Geochronology Centre Special Publication 5.

Paton, C., Hellstrom, J., Paul, B., Woodhead, J., Hergt, J., 2011. Iolite: Freeware for the visualisation and processing of mass spectrometric data. *Journal of Analytical Atomic Spectrometry*, 26, 2508-2518.

Pearce N.J.G., Perkins, W.T., Westgate, J.A., Gorton, M.P., Jackson, S.E., Neal, C.R., Chenery, S.P., 1997. A compilation of new and published major and trace element data for NIST SRM 610 and NIST SRM 612 glass reference materials. *Geostandards Newsletter*, 21, 115-144.

Rubatto, D., Williams, I.S., Buick, I.S., 2001. Zircon and monazite response to prograde metamorphism in the Reynolds Range, central Australia. *Contributions to Mineralogy and Petrology*, 140, 458-468.

Schmitz, M.D. Schoene, B., 2007. Derivation of isotope ratios, errors, and error correlations for U-Pb geochronology using ^{205}Pb - ^{235}U -(^{233}U)-spiked isotope dilution thermal ionization mass spectrometric data. *Geochemistry Geophysics Geosystems*, 8, Q08006.

Spandler, C., O'Neill, H.StC., Kamenetsky, V.S., 2007. Survival times of anomalous melt inclusions from element diffusion in olivine and chromite. *Nature*, 447, 303-306.

Spandler, C., Pettke, T., Rubatto, D., 2011. Internal and External Fluid Sources for Eclogite-facies Veins in the Monviso Meta-ophiolite, Western Alps: Implications for Fluid Flow in Subduction Zones. *Journal of Petrology*, 52, 1207-1236.

Stacey, J.S., Kramers, J.D., 1975. Approximation of terrestrial lead isotope evolution by a two-stage model. *Earth and Planetary Science Letters*, 26, 207-221.

Steck, A., Della Torre, F., Keller, H., Pfeifer, H.-R., Hunziker, J., Masson, H., 2013. Tectonics of the Lepontine Alps: Ductile thrusting and folding in the deepest tectonic levels of the Central Alps. *Swiss Journal of Geosciences*, 106, 427-450.

Todd, C.S., Engi, M., 1997. Metamorphic field gradients in the Central Alps. *Journal of metamorphic Geology*, 15, 513-530.

von Blanckenburg, F., 1992. Combined high-precision chronometry and geochemical tracing using accessory minerals: applied to the Central-Alpine Bergell intrusion (central Europe). *Chemical Geology*, 100, 19-40.

Williams, I.S., 1998. U-Th-Pb Geochronology by Ion Microprobe. In M.A. McKibben, W.C. Shanks III, W.I. Ridley (Eds.), Applications of microanalytical techniques to understanding mineralizing processes. Reviews in Economic Geology, 7, 1-35.

Supplementary Tables captions

Table A1: Major and trace element whole rock compositions by XRF (wt %) and LA ICPMS (ppm).

Table A2. Representative garnet major and trace element analyses.

Table A3. Rutile trace element analyses (measured by LA-ICP-MS; internal Standard TiO₂=98 wt%).

Table A4. Allanite major and trace element analyses (measured by EDS and WDS - major - and LA-ICP-MS - traces). Concentrations are in oxide wt % for major elements and ppm for trace elements.

Table A5. Monazite major and trace element analyses (measured by LA-ICP-MS). Concentrations are in ppm when not otherwise specified

Table A6. Monazite U-Th-Pb analyses measured by SHRIMP ion microprobe.

Table A7. Allanite U-Th-Pb analyses measured by SHRIMP ion microprobe.

Table A8. Results of TIMS analysis of rutile and description of grain fractions. ²⁰⁶Pb/²⁰⁴Pb ratios are corrected for spike and fractionation only. Radiogenic ratios are corrected for spike, fractionation and initial Pb using the K-feldspar composition. Data were reduced and errors propagated using AnySpike (Schmitz and Schoene, 2007).

Table A8b. Measured Pb isotopic composition of low-U-feldspar